JGR Earth Surface

RESEARCH ARTICLE
10.1029/2023JF007556

Special Collection:
The Arctic: An AGU Joint Special Collection

Life Cycles and Polycyclicity of Mega Retrogressive Thaw Slumps in Arctic Permafrost Revealed by 2D/3D Geophysics and Long-Term Retreat Monitoring

Michael Krautblatter[1], Michael Angelopoulos[1,2,3], Wayne H. Pollard[3], Hugues Lantuit[2,4], Josefine Lenz[2,5], Michael Fritz[2], Nicole Couture[6], and Saskia Eppinger[1]

[1]Chair of Landslide Research, TUM School of Engineering and Design, Technical University of Munich, Munich, Germany, [2]Alfred Wegener Institute Helmholtz Centre for Polar and Marine Research, Potsdam, Germany, [3]Department of Geography, McGill University, Montreal, QC, Canada, [4]Institute of Geosciences, University of Potsdam, Potsdam, Germany, [5]Institute of Northern Engineering, Water and Environmental Research Center, University of Alaska Fairbanks, Fairbanks, AK, USA, [6]Geological Survey of Canada, Natural Resources Canada, Ottawa, ON, Canada

Key Points:

- Mega retrogressive thaw slumps develop polycyclic behavior as material is thermally and mechanically prepared for future generation failures
- Geophysical images show decameter-deep thermal perturbations by warm, wet mud deposition, gully incision, and lateral slumping along gullies
- We provide a summary classification of polycyclic reworking stages based on electrical resistivity tomography and ground-penetrating radar structures and geomorphological features

Correspondence to:
M. Krautblatter,
m.krautblatter@tum.de

Citation:
Krautblatter, M., Angelopoulos, M., Pollard, W. H., Lantuit, H., Lenz, J., Fritz, M., et al. (2024). Life cycles and polycyclicity of mega retrogressive thaw slumps in Arctic permafrost revealed by 2D/3D geophysics and long-term retreat monitoring. *Journal of Geophysical Research: Earth Surface*, *129*, e2023JF007556. https://doi.org/10.1029/2023JF007556

Received 6 DEC 2023
Accepted 7 JUN 2024

Abstract Mega retrogressive thaw slumps (MRTS, $>10^6$ m^3) are a major threat to Arctic infrastructure, alter regional biogeochemistry, and impact Arctic carbon budgets. However, processes initiating and reactivating MRTS are insufficiently understood. We hypothesize that MRTS preferentially develop a polycyclic behavior because the material is thermally and mechanically prepared for subsequent generation failure. In contrast to remote sensing, geophysical reconnaissance reveals the inner structure and relative thermal state of MRTS decameters beneath slump surfaces, potentially controlling polycyclicity. Based on their life cycle development, five (M)RTS were studied on Herschel Island, an MRTS hotspot on the Canadian Beaufort coast. We combine >2 km of electrical resistivity tomography (ERT), 500 m of ground-penetrating radar (GPR) and annual monitoring of headwall retreat from 2004 to 2013 to reveal the thermal state, internal structure, and volume loss of slumps. ERT data were calibrated with unfrozen-frozen transitions from frost probing of active layer thickness and shallow boreholes. In initial stage MRTS, ERT displays surficial thermal perturbations a few meters deep, coincident with recent mud pool and mud flow development. In early stage polycyclic MRTS, ERT shows decameter deep-reaching thermal perturbations persisting even 300 years after the last activation. In peak-stage polycyclic MRTS, 3D-ERT highlights actively extending deep-reaching thermal perturbations caused by gully incisions, mud slides and mud flows. GPR and headwall monitoring reveal structural disturbance by historical mud flows, ice-rich permafrost, and a decadal quantification of headwall retreat and slump floor erosion. We show that geophysical signatures identify long-lasting thermal and mechanical disturbances in MRTS predefining their susceptibility to polycyclic reactivation.

Plain Language Summary Mega retrogressive thaw slumps, hereafter slumps, are a giant type of erosional landform linked to permafrost thaw. They endanger Arctic infrastructure and are an important source of carbon emission in the Arctic. Processes that initiate and reactivate slumps are poorly understood. To better understand the internal structures and processes, we used geophysical techniques to study five slumps in a hotspot area on Herschel Island, YT, Canada. We compared geophysical measurements with field measurements of slump erosion (2004–2013) to gain information about the internal structures and material volume loss. In the initial slump stage, geophysical methods show shallow thawing underneath recent mud pools and mud flows. Reactivated slumps show deep reaching thermal influences in an early stage of development that can still be detected 300 years after the last activation. Highly active reactivated slumps show deep-reaching thermal disturbances caused by gully incisions, organic layer removal, mud slides and mud flows. The applied methods can show the influence of former mud flows and ice-rich permafrost and how they persist over decades and prepare slumps for future reactivation. Here we show that geophysical methods can be used to identify long-lasting thermal and mechanical disturbances in slumps that predefine their likelihood for reactivation.

1. Introduction

Mega retrogressive thaw slumps (MRTS) supply large amounts of sediment and organic carbon to the nearshore zone and are a serious risk for Arctic infrastructure. These MRTS are also indicators of climate warming and permafrost degradation (Turetsky et al., 2020), even in very cold regions of the High Arctic (Lewkowicz &

Figure 1. Components of mega retrogressive thaw slumps exemplified by Slump D on Herschel Island (2012). Headwalls greater than 10 m high and massive mud flows govern the energy uptake and thawing of ice-rich materials. Upon thaw, the initially salt-rich mud loses ice-bonding and salt-bonding strength, leading to flowing mud with a friction angle of a few degrees.

Way, 2019; Olefeldt et al., 2016; Segal et al., 2016; Ward Jones et al., 2019). Retrogressive thaw slumps (RTS) are a form of back-wasting thermokarst initiated from a scarp or headwall following natural or anthropogenic disturbance. Natural exposure mechanisms include coastal erosion, lake shore erosion, slope undercutting by a river, slope failure and associated massive ice exposure. Structural components (Figure 1) of thaw slumps include a slump floor consisting of a viscous mud pool, an ablating ice-rich face and a vertical headwall consisting of a permafrost layer of less ice-rich sediment and an active layer (Lantuit & Pollard, 2005). Large RTS, so called MRTS have several meters to decameters high ablating ice-rich faces, extend for hundreds of meters, and contain thick massive ground ice structures (Fritz et al., 2011). Besides being a major threat to Arctic infrastructure, RTS are one of the most important abrupt release mechanisms of organic carbon in permafrost areas (Rachold et al., 2000; Tanski et al., 2017; Turetsky et al., 2020). It has been shown that RTS are a major contributor to lateral carbon fluxes along the entire Arctic coastline (Lantuit et al., 2009; Ramage et al., 2018, 2019) and into freshwater ecosystems (Kokelj et al., 2013, 2015, 2021; Littlefair et al., 2017). Several studies have provided evidence for accelerating RTS activity with climate change (Kokelj et al., 2015; Lantz & Kokelj, 2008; Lewkowicz & Way, 2019; Ward Jones et al., 2019). Our study was carried out in a global hotspot area for RTS activity (Kokelj et al., 2017) where retrogressive thaw slump area increased three-fold since 1952 (Lantuit & Pollard, 2008; Ramage et al., 2018).

The generation and activity of RTS are controlled by several promoting and reinforcing factors. RTS preferentially develop in sloping terrain characterized by susceptible materials such as fine-grained permafrost sediments along coasts and rivers and containing massive ground ice (Lewkowicz, 1987b; Ramage et al., 2017). Leibman et al. (2008) suggested that the scales of slumps are governed by the presence of massive ice. In Eastern Siberia, RTS are mostly developed in the Yedoma (Pleistocene-aged) Ice Complex (Leibman et al., 2008; Opel et al., 2019). In the western Canadian Arctic, active RTS develop mostly in ice-rich formerly glaciated landscapes (Rudy et al., 2017).

According to the thaw consolidation theory, there is a balance between thawing and drainage in ice-rich soils (Morgenstern & Nixon, 1971). General controls on ablation rates include net radiation flux, sensible and latent heat fluxes at the surface, as well as the sediment thermal regime, snow precipitation and cover, debris flows, and water flowing down the ice face (Lewkowicz, 1987a; Pufahl & Morgenstern, 1979; Zwieback et al., 2018). The slope face aspect is also important, as RTS in central Yakutia mainly occur along south to south-west facing banks due to solar radiation and higher air temperatures (Lacelle et al., 2015; Séjourné et al., 2015).

The exposure and cliff height of slump headwalls are in part governed by slope erosion (Are et al., 2005). If the thawed material is removed from the foot of the slope, continued thawing of ice-rich sediments and massive ice along the headwall can persist over decades or longer, like the Batagay slump in central Yakutia (Kizyakov et al., 2023; Murton et al., 2023; Shepelev et al., 2020). MRTS headwalls can retreat from meters to decameters per year on the Yukon coast (Obu et al., 2017), the western coast of Kolguyev Island (Kizyakov et al., 2013) as well as central Yakutia in Russia (Opel et al., 2019). Thawed supersaturated material often collects decimeter to more than a meter-deep mud pools (De Krom & Pollard, 1989; Lantuit & Pollard, 2005) that form at the base of the headwall and periodically release mud flows (Lantuit & Pollard, 2008; Lewkowicz, 1988) (Figure 1). If drainage and material removal at the shoreline cannot keep pace with the supply of thawed material, slump activity can cease as the ice face becomes covered and insulated by surface layers due to an increase in overburden thickness and a decrease in the slope angle (De Krom, 1990; Lewkowicz, 1987a, 1988).

To understand and model future MRTS activity and its importance for Arctic carbon budgets, polycyclicity is a key phenomenon (Table 1, Figure 2). Polycyclicity is the reoccurrence of an RTS at the same location as before and therefore the subsequent potential occurrence of several generations of slumps simultaneously. Up to 90% of currently active thaw slumps observed in the Canadian Arctic occur as polycyclic slumps in former slump floors (Lantuit & Pollard, 2005; Mackay, 1966; Ramage et al., 2018). The main driver of polycyclicity is the capacity of the slump to reactivate, which is controlled by (a) the preservation of ice-rich sediments under the slump floor and (b) the redeposition of these sediments at the bottom of the slump. Both lead to thermal perturbation (i.e.,

Table 1
Retrogressive Thaw Slump Development Stages and Associated Geomorphological Processes (Later Complemented by Table 2: Geophysical Signatures and Table 3: Synthetic Table)

	Typical Active Slump Age [a] (Lantuit & Pollard, 2005, 2008)	Process and Development Stage	Example
0a. Undisturbed tundra			
0b. Dormant stage		Visible historic headwall at least in a part of the slump	Collinson Head (western half), Figure 6
1. Initial polycyclic reworking stage	10^0–10^1	• Initial mud pool development • Headwall 10^0–10^1 m • Length/width 10^1 m • Single lobe structure	Collinson Head (eastern half), Figure 6
2. Peak polycyclic reworking stage	10^1–10^2	• Massive mud pool • Headwall 5–30 m • Length/width 10^1–10^2 m • Multiple lobe structure	Slumps A, B, C, Figure 2
3. Super-polycyclic expansion	10^1–10^2+	• Coalescence of multiple peak polycyclic stage slumps • Widespread expansion beyond old headwall into undisturbed tundra • Only certain slumps reach this stage • Intense meltwater discharge from the headwall and massive gullying on the slump floor	Slump D (Figure 11); C & A (in transition from stage 2–3)

erosional and depositional processes disturbing the thermal regime), which acts against the preservation of ice-rich sediments and therefore modifies the position of the preserved ice-rich sediments in relation to the shoreline (Lantuit et al., 2012). Polycyclicity is commonly attributed to (a) thermal disturbance, for example, the exposure of massive ice or ice-rich permafrost, (b) geomorphological processes, for example, active layer detachments, rivers, gullying and coastal erosion and (c) mechanical preconditioning, for example, salt-rich fine-grained frozen materials which lose initial strength upon mud flow mobilization. These lost salt-bonding effects are not regained upon redeposition. Salt-induced thixotropy, which has been tested in the laboratory (Perret et al., 1996), can persist for hundreds of years until salt bonds re-develop their initial strength. The widespread appearance of gullying and lateral slumping, that is, rotational slope failures along gullies and shorelines is presumably (d) a combination of (a)–(c) and is more common for large slumps with significant meltwater discharge and mud flows from the headwall (Figure 2).

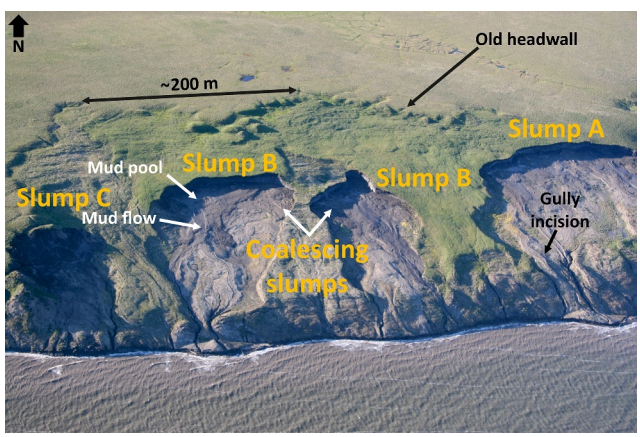

Figure 2. Life cycles and polycyclicity of mega retrogressive thaw slumps (MRTS) in summer 2006. Slumps A, B, and C are second-generation retrogressive thaw slumps, and start to currently form an MRTS peak polycyclic reworking stage with gully incisions, mud flows, and mud pools downslope of the headwall. Once the current slump retreats beyond the old headwall, it is considered to be in a phase of super-polycyclic expansion.

Geophysical reconnaissance by GPR or electrical resistivity tomography (ERT) has the capability to detect changes in subsurface structure and unfrozen/frozen sediment transition meters to decameters below the ground surface, respectively. ERT has become a common method to investigate permafrost and thermokarst phenomena (Angelopoulos et al., 2021; Kunz et al., 2023; You et al., 2017) but has so far not been applied to study the thermal evolution and polycyclicity of RTS.

During (a) initial polycyclic reworking, mud pools develop under head walls a few meters high and reactivate the RTS. The processes redistributing water, energy and material on the slump surface occur in a single lobe; initial polycyclic reworking is a common phenomenon. Some polycyclic MRTS expand toward a (b) peak polycyclic reworking stage, characterized by 5–30 m high and extensive headwalls, and several mud pools a meter-deep and multiple often interlinked lobe structures generated by massive water, energy and material redistribution. A few MRTS may even extend the area beyond their former RTS area, which we refer to (c) as "super-polycyclic" expansion. Figure 2 and Table 1 illustrate and define the stages of polycyclic reworking.

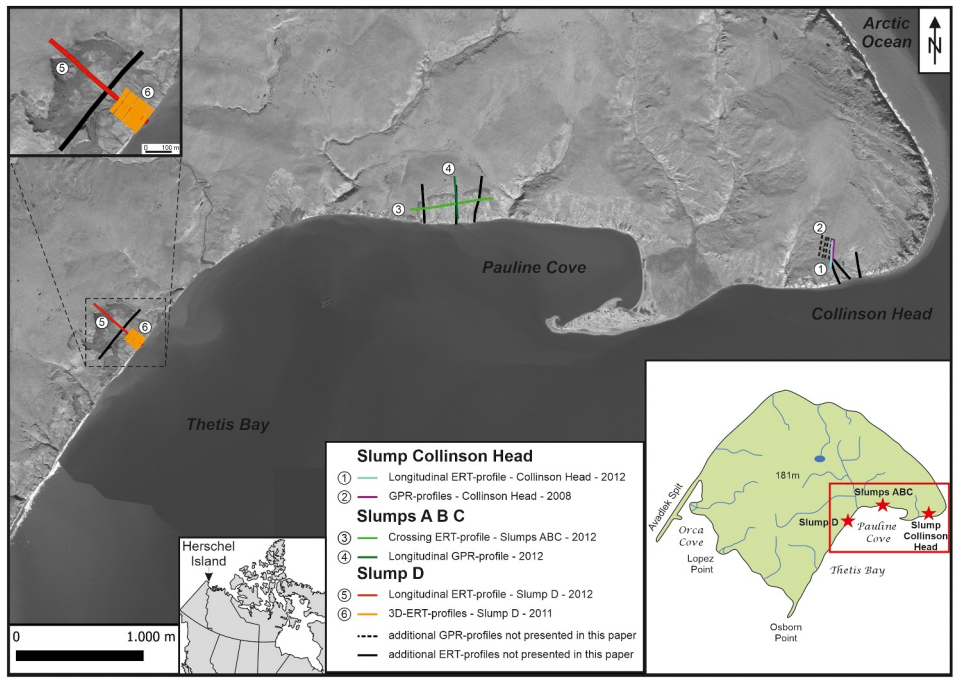

Figure 3. 2D and 3D geophysical profiles in the five selected retrogressive thaw slumps on Herschel Island, inset map modified from Fox (2012), background DEM: 2011.

This study provides decameter-deep geophysical insights into all stages of polycyclic MRTS development on Herschel Island (Yukon, Canada) and reveals information on the thermal and mechanical conditions controlling polycyclicity. We hypothesize that:

1. The spatial scale of polycyclicity is not solely related to ablation dynamics at the headwall and the bottom of the slump but also by heat transmission during mud transport and deposition.
2. The coupled mechanical and thermal recovery of material transported by MRTS takes decades to hundreds of years and determines the time scale of polycyclicity.
3. Reactivation through coastal dynamics is not restricted to mechanical erosion but also occurs due to toe instability caused by saltwater intrusion and thermal disturbances by gullies and lateral slumping along them.

2. Study Site

Herschel Island - Qikiqtaruk is an island located 3 km off the mainland of the Yukon coast in the Canadian Beaufort Sea (69°34′N, 138°55′W; Figure 3). With an area of about 110 km^2 and maximum elevation of 183 m a.s.l., the island is composed of highly deformed glacial, marine, and terrestrial sediments (Fritz et al., 2012; Rampton, 1982). These were excavated from the shelf and deposited as a push moraine by the final advance of the Laurentide Ice Sheet (Mackay, 1959) during the last Wisconsin Glacial Period (Fritz et al., 2012; Rampton, 1982), resulting in elevated salt content (Kokelj et al., 2002). Moraines within the Late Wisconsin Laurentide ice limit often include buried glacier ice and massive segregated ice (French, 1998; Fritz et al., 2011). This leads to highly variable ground-ice contents in fine-grained, matrix-based diamictons (Fritz et al., 2012). Also, the fine-grained unconsolidated sediments on Herschel Island frequently include massive bodies of ground ice, often several meters thick and extending for hundreds of meters (Bouchard, 1974; Fritz et al., 2011, 2012; Pollard, 1990). Abundant Holocene ice wedge development has also been intensively investigated on Herschel island (Fritz et al., 2016). Glacially upthrusted marine sediments are characterized by high pore-water electrical conductivities up to 50 mS/cm in the central Mackenzie Delta (Kokelj et al., 2002) and up to 15 mS/cm on Herschel Island (Fritz et al., 2012).

The mean annual air temperature 50 km west of Herschel Island at Komakuk Beach was about −11°C and the mean annual precipitation was 161 mm for the period 1971–2000 (Environment Canada; http://climate.weather.

gc.ca). The mean annual ground temperatures at 1 m depth have been shown to vary from −4.0 to −9.0°C, and the depth of the zero annual amplitude was estimated to be 14.5 m, with a temperature of −8.0°C (Burn & Zhang, 2009). Permafrost in the area is continuous and can reach depths of 300 m (Smith & Burgess, 2000). The active layer thickness usually ranges from 30 to 90 cm depending on topography. Burn and Zhang (2009) compared the present-day climate to historical climate records (1899–1905) and determined warming at the top of the permafrost of more than 2°C; they inferred that these ground perturbations have already reached 120 m depth.

Due to the projected rise in relative sea level, increasing storminess, and longer open water seasons, as well as increasing sea surface and air temperatures, Herschel Island is likely to experience greater coastal erosion.The average recorded coastline retreat on Herschel Island was 0.68 ma^{-1} for the period 2000–2011 (Obu, Lantuit, Fritz, Pollard, et al., 2016). Erosion rates increased by more than 50% in comparison with the period 1970–2000 (Lantuit & Pollard, 2008; Obu, Lantuit, Fritz, Pollard, et al., 2016). From 1952 to 2011, the number of active RTS around the Herschel Island coasts increased from 46 to 99 (Lantuit & Pollard, 2008; Ramage et al., 2017). Lantuit et al. (2012) studied the polycyclicity of RTS and showed that they were particularly active approximately 300 years before present (BP). RTS are currently undergoing a similar period of enhanced activity where climate warming could shorten the time span until renewed activity, leading to higher frequencies of RTS activity in the future (Lantuit et al., 2012).

We selected three adjacent well-studied thaw slump environments in different stages of development (Table 1), including Slumps ABC, Slump D, and Collinson Head (Figure 3). Here, we introduce the basic geomorphological characteristics of the slumps for the years 2012 and 2013, during which we performed all geophysical surveys listed in this paper. Collinson Head is a small RTS measuring 100 m wide at the slump floor located at the eastern tip of the Island (also called Collinson Head). However, the active portion of the slump in 2012 measured just 25 m wide and the headwall was only 2 m high. Collinson Head is an example of an initial polycyclic reworking stage where past disturbance is evident from aerial imagery, vegetation surveys (Cray & Pollard, 2015), and the geophysical data presented here. Collinson Head is characterized by a single lobe structure, an initial mud pool, and small mud flow deposits.

In 2013, Slumps ABC represented a peak polycyclic reworking stage with each slump (A, B, and C) beginning to retreat into a larger pre-existing thaw slump body (Table 1). The former headwall is clearly visible as a densely vegetated low angle scarp in Figure 1 dated 300 years BP (Lantuit et al., 2012). Slumps A and B measure approximately 200 m across and Slump C is 50 m across. The maximum headwall height in 2013 was approximately 8 m for Slump B, 5 m for Slump A, and 4 m for Slump C. These slumps are characterized by multiple lobes, massive mud pools, and the initial formation of thermo-erosional gullying on the slump floors.

Slump D is located 3 km further west on the coast of Thetis Bay. Slump D represents a stage of a super-polycyclic expansion (Table 1) extending beyond its historic limits. It is over 500 m wide and had a maximum headwall height exceeding 20 m in 2012, thus being one of the largest-known RTS in the Arctic. This slump is characterized by the coalescence of multiple slumps in their peak polycyclic reworking stage as well as extensive thermo-erosion gullying with massive mud flows.

3. Methods

3.1. ERT Transects

In 2011 and 2012, 30 ERT transects were measured on the five selected (M)RTS (Figure 3). We used an ABEM SAS 300C resistance meter with an ES 464 electrode selector connected to two 5 m spacing cables with 21 electrodes each. Marine and glacial fine-grained and salt-rich sediments provided excellent electric coupling of the ca. 20 cm long steel electrodes and facilitated high pre-selected currents of ≥10 mA.

In 2D surveys, cables were arranged in roll-along surveys, where electrode cables were repeatedly added at one end of the survey to extend it up to 650 m length. First, 2D surveys were carried out in undisturbed tundra along active layer depth profiles generated from permafrost probe measurements. This is because in undisturbed tundra the ERT unfrozen-frozen transition can easily be validated with permafrost probe depths of 0–1 m while this is impractical for greater thaw depths in mega slumps. Electrode coupling in muddy soil generated very low contact resistances in the range of less than 1 ohm to a few ohms, providing consistent ERT measurements with low errors. This allowed us to calibrate the ERT results by determining the resistivity for an unfrozen to frozen transition. The 2D ERT surveys were systematically generated as longitudinal profiles starting in undisturbed

tundra above the headwall of the MRTS and following the altitudinal gradient until the lower end of the MRTS or the coastline was reached. This was carried out for Collinson Head, Slumps ABC, as well as Slump D. Transverse profiles were generated in the larger slumps (A, B, C, and D), and where multiple slumps coalesced. These transects were extended into the surrounding tundra beyond the slump scars. In the largest RTS, Slump D—an MRTS, we also applied 3D ERT to characterize the thermal impact of mud flows, creeks, thermally induced landsliding, and coastal erosion. This quasi-3D ERT survey was designed as a combination of seven 100 m long transverse ERT sections with 2.5 m electrode spacing, starting parallel to the shoreline at a 15 m distance, with subsequent profiles measured at 35, 55, 75, 95, 115, and 135 m distances from the shoreline. The relative topography along the profiles was measured at every electrode with a high-precision inclinometer (Necli) and was referred to known differential global positioning system (DGPS) points every 100 m or shoreline positions. We used a combined Wenner-Schlumberger-Array for all profiles except the 3D ERT survey in Slump D, where only a Wenner-Array configuration was used.

ERT profiles were inverted using the standard ERT software RES2DINV ver. 4.10.4. We applied a robust inversion and mesh refinement, as these settings delivered significantly better uncertainty distributions at depth in comparison to standard inversion settings. For all calculated profiles, we used a robust inversion to allow a better inversion of the model along the sharp resistivity gradients of frozen bodies. The number of iterations used was determined by a RMS error smaller than 2% between two iterations.

The applied Wenner-Array configuration accurately detects horizontally layered resistivity contrasts but is insensitive to sharp vertical resistivity structures (Telford et al., 1990). Vertical resistivity structures occur for instance at the transition from warm mud to vertical ice walls bridging two 2–3 magnitudes of resistivity. We hereafter highlight/camouflage potential artifacts in the respective figures, particularly beneath mud pools. However, the raw apparent resistivites under the mud pools revealed unique characteristics prior to the inversion process, hinting that the mud pools had a thermal effect on the subsurface. Analyzing the raw apparent resistivity prior to inversion is a useful approach to avoid the misinterpretation that would result from inversion-generated artifacts (Alumbaugh & Newman, 2000; Krautblatter, 2010).

3.2. Frost Probing

To calibrate the ERT measurements and determine the active layer thickness, manual frost probing was implemented parallel to 3 ERT profiles in undisturbed tundra in August 2012. Therefore, a 120 cm-long mechanical frost probe was pushed into the active layer until the permafrost table was reached. The probing was carried out midpoint between the electrodes, leading to 40 measurements per profile with a spacing of 0.25, 1, and 4 m, depending on ERT profile length of 10, 40, and 160 m, respectively.

3.3. GPS Monitoring

From 2004 to 2012 at Collinson Head, and from 2004 to 2013 at Slumps ABC, DGPS surveys of slump headwalls were carried out every year (except 2005) in late summer with a Trimble 4700. The headwall position was recorded every few meters and annual headwall retreat rates were then calculated. In 2012 and 2013, coastal LiDAR data were collected (Obu, Lantuit, Fritz, Grosse, et al., 2016). From this data, 1 m ground surface resolution digital elevation models (DEM) were derived for the slump floors, headwalls, and surrounding tundra for Collinson Head and Slumps ABC. The 2013 DEM was compared to a 2 m ground surface resolution DEM from 18 September 2004 in Esri ArcGIS software. The 2004 DEM is a PhotoSat product created using a proprietary stereo image matching process with IKONOS satellite images. The reader is referred to Obu et al. (2017) for detailed information on the 2013 LiDAR product. To perform the comparison, the 2013 DEM was first resampled to a 2 m grid size using ESRI ArcGIS software and a bilinear interpolation. Site-specific offsets between the 2013 resampled LiDAR and 2004 DEM were calculated for undisturbed terrain segments above Slumps ABC and Collinson Head by subtracting the 2013 resampled LiDAR from the 2004 DEM at 2 m intervals. The mean offsets for Slumps ABC and Collinson Head were 3.4 and 4.8 m, with standard deviations of 0.2 and 0.3 m, respectively. Typically, stable terrain features such as gravel pads are used to compare DEM offsets (Jones et al., 2013). Since such features were not available, we selected sites of undisturbed tundra with no observed subsidence or ground surface flows from 2004 to 2013 as an alternative. The 2004 DEM data set was modified based on the calculated offsets, once for slumps ABC and once for Collinson Head. Finally, we subtracted the resampled 2013 LiDAR image from the modified 2004 DEM to generate 3D estimates of net volume loss (sediment and ice) from slump

Table 2
Mega Retrogressive Thaw Slump Development-Stage Related Features Documented in the Geophysical Reconnaissance

		Collinson Head	Slumps A, B, C	Slump D
(1) Unfrozen extended surface layer (i.e. deeper than modern day active layer in undisturbed tundra)	(1a) Only under active unvegetated slump floor	X		
	(1b) even persistent under less active vegetation succession areas		X	X
(2) Ice-rich permafrost under	(2a) slump floors	X	X	X
	(2b) tundra	X	X	X
(3) Mud pool		X	X	X
(4) Tundra	(4a) previously disturbed	X	X	X
	(4b) undisturbed	X	X	X
(5) Sub-sea level low resistivity zone			Partly X	X
(6) Excessive gully and lateral sliding zone				X

activity. The results are referenced to individual slump extents from 2004 to 2013 based on the DGPS headwall extents. Since the 2004 headwall position was measured on 8 August 2004, the headwall position of the 2004 DEM was situated further inland. Therefore, substracting the 2013 DEM from the modified 2004 DEM can result in negative values beyond the 18 September 2004 headwall extent due freshly deposited slump material. For simplicity, we only display material loss in the map results.

3.4. GPR

In 2012, we carried out a 300 m long 50 MHz GPR survey between Slump A and Slump B to evaluate the internal structure of permafrost as it transitions from a former slump floor to undisturbed tundra. The geomorphological evidence of past slump activity is visible through densely vegetated scarps further inland than the current headwall (Figure 1). This survey is a crucial calibration step for mapping structural inhomogeneity in permafrost at slumps such as Collinson Head, where past disturbance is not easily topographically apparent at the surface. In 2008, 50 MHz GPR surveys were undertaken perpendicular to the headwall at Collinson Head. The survey presented in this paper started just above the 2008 headwall position and proceeded 150 m further inland. We used a MALA Geoscience unshielded rough terrain antenna with a transmitter-receiver separation of 4 m. Although the rough terrain antenna has a poor near-surface resolution in comparison to a standard antenna system, it was logistically expedient and necessary over the hummocky tundra. The data were processed with EKKO Project software (Sensors & Software). After re-picking the first break, a dewow filter followed by an exponential gain compensation function was used for the profiles. In addition, a background subtraction filter was applied to the data using the window size of the profile length. For time to depth conversion, a typical permafrost signal velocity of 0.12 m/ns was used. To correct for topography, differential GPS measurements (Trimble 4700) were recorded approximately every 10 m on the survey line between Slump A and Slump B. The Collinson Head profile topography was taken from the modified 2004 DEM.

4. Results

This section describes geophysical signatures indicative of different stages of retrogressive thaw slump development. The transects have been aligned according to prior geomorphological and vegetation succession mapping by the authors to include representative, well-developed and appropriately scaled features indicative for mass and energy fluxes in different stages of slump evolution (Table 2).

4.1. ERT and GPR Calibration in Undisturbed Tundra

We performed an accurate calibration of ERT surveys in undisturbed tundra compared to parallel frost probing (see chapter 3.2) with a 0.25 m electrode spacing and frost probe spacing resolution, which is shown in Figure 4. The measurements for active layer thickness varied between 20 and 55 cm in August 2012. In the upper 50 cm, the

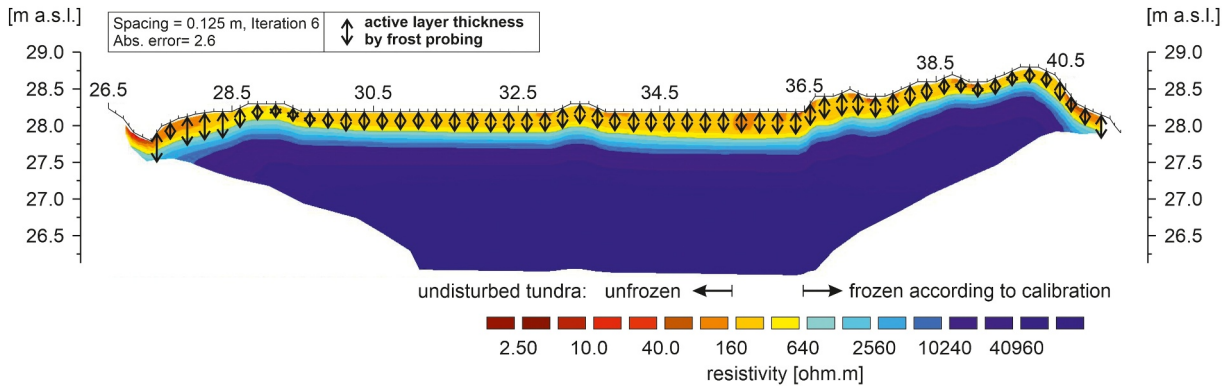

Figure 4. Electrical resistivity tomography (ERT) calibration survey in undisturbed tundra, where permafrost probing measurements verified the active layer depth and thus the thaw-freeze transition of the ERT.

electrical resistivity varied between 300 and 600 Ωm. At 50 cm depth, there is a consistent sharp transition to ≥1,000 Ωm, matching well with the permafrost probe depth. Below, ERT values consistently and gradually increase to 40,000 Ωm at 2 m depth, corresponding to colder ice-rich permafrost conditions.

For GPR, surveys from previously disturbed to undisturbed tundra were carried out between Slumps A and B (Figure 5). At the headwall, located 260 m from the survey start (Figure 5), there is a clear transition from relatively thick-layered sediment to a thin veneer of sediment overlying chaotic hyperbolic reflections. In previously disturbed tundra, along the former slump floor ≤260 m, hyperbolic reflection events were less frequent compared with the undisturbed tundra upslope of 260 m.

4.2. Initial Polycyclic Reworking Stage (Collinson Head)

At Collinson Head, the ERT surveys below the active headwall showed a 2.5–5.0 m thick reddish to orange layer of apparently unfrozen (acc. to calibration) material with resistivities ranging from 20 to 100 Ωm (Figure 6). Below this unit, the resistivities increased gradually in a consistent layer from 1 kΩm (aqua) to 5 kΩm (light blue) 6–10 m below the ground surface, which is interpreted as the upper limit of permafrost according to the calibration, reaching values ≥20 kΩm at greater depths. Just below the active headwall at the location of the mud pool, there appeared to be a low resistivity bulb of 300 Ωm dipping to 5 m below the slump floor, possibly exaggerated in depth due to geometrical constraints in the inversion. In between the 2012 active headwall position

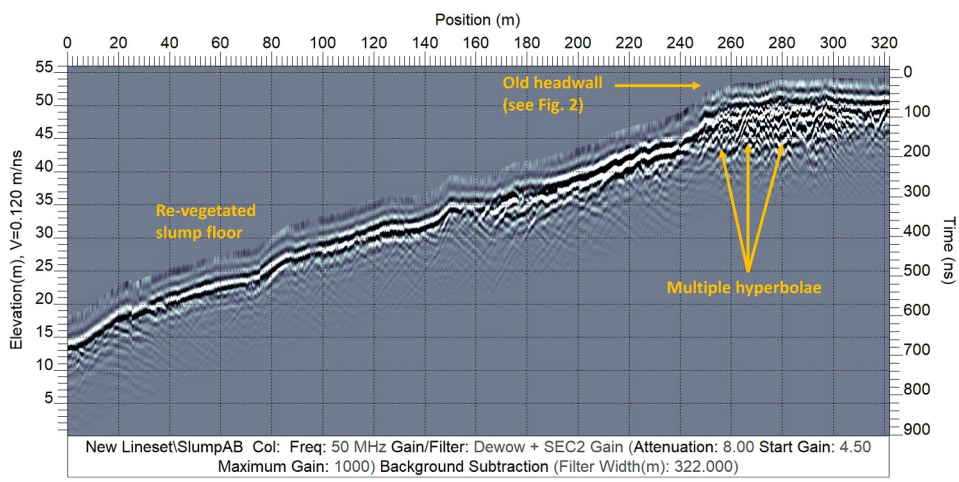

Figure 5. 50 MHz ground-penetrating radar survey showing transition from a former slump floor to undisturbed tundra between Slumps A and B (Profile 4 in Figure 3). The start of the survey (position 0 m) was located toward the toe of the re-vegetated slump floor in between Slumps A and B at an elevation of 18 m above sea level. The background subtraction filter suppresses the direct air and ground wave arrivals.

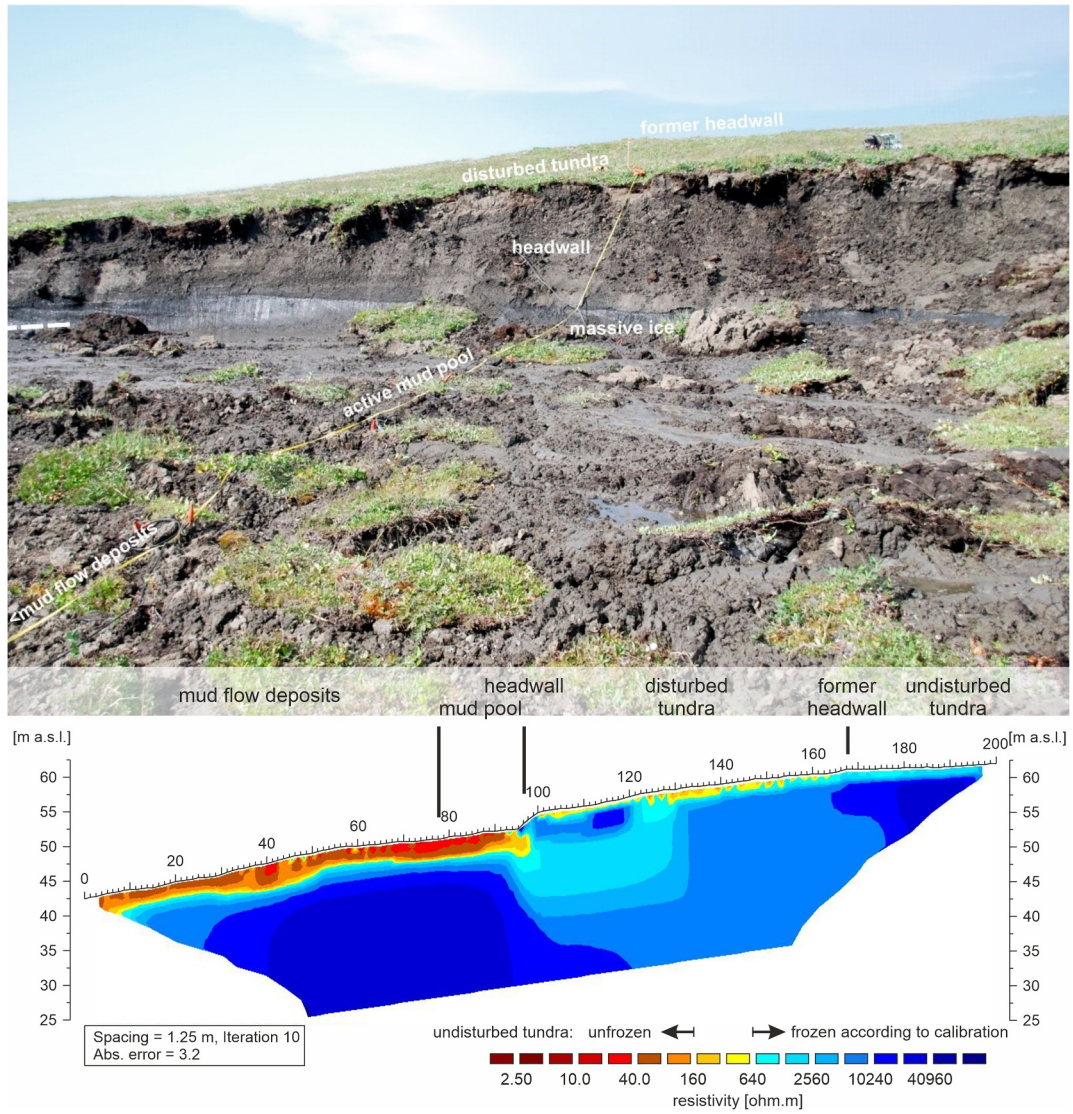

Figure 6. Top panel: Slump at Collinson Head showing electrical resistivity tomography (ERT) survey set up in 2012 at the transition from the slump floor to above the headwall. Bottom panel: Inverted ERT survey results. For position, refer to Profile 1 in Figure 3. The calibration is according to Figure 4 and Section 4.1.

and 40 m upslope of the headwall, the low resistivity unit just below the surface was more resistive (160–320 Ωm) and half the thickness (maximum 2.5 m depth) compared to the low resistivity unit downslope of the 2012 headwall. (a) Above the morphologically visible former headwall that is, 170 m we find subsurface values in >5 m depth with values >10 kΩm consistent with undisturbed tundra. (b) From 90 to 170 m in >5 m we find values mostly between 1 and 10 kΩm consistent with previously disturbed tundra. (c) From 30 to 90 m in >5 m resistivity values are unexpectedly high in the range from >10 kΩm. From nearby exposures in Collinson Head we know that this corresponds to a band of a very ice-rich unit persistent perpendicular to the slope angle. Further upslope, the low resistivity unit at the ground surface gradually increased in resistivity and decreased in thickness at the end of the survey line. In addition, the resistivity of the highly resistive structure underneath gradually increased until reaching a maximum value of 20 kΩm at the end of the survey line (≥170 m) close to where increased hyperbolic reflection patterns are apparent in the GPR profile.

In the 50 MHz GPR survey (Figure 7), the structural features revealed from the GPR shifted at the 70–100 m positions from parallel continuous reflections to chaotic patterns characterized by multiple hyperbolas. This

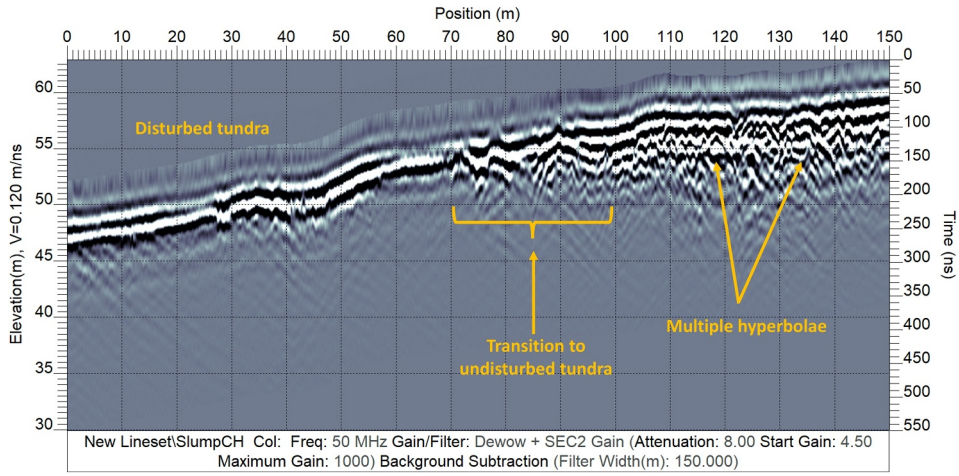

Figure 7. A 50 MHz ground-penetrating radar (GPR) survey at Collinson Head parallel to the electrical resistivity tomography (ERT) in Figure 6 was measured in 2008. The start of the survey (Position 0 m) was located on the tundra above the 2008 headwall position at an elevation of 52 m above sea level. As a result, this profile did not intersect a slump floor or active headwall in 2008. As the slump retreated, the tundra at the beginning of the 2008 survey line was eroded. For the position, see Profile 2 in Figure 3. The position 0 m on the 2008 GPR profile corresponds to position 60 m in the 2012 ERT profile. The background subtraction filter suppresses the direct air and ground wave arrivals.

transition is very similar to the structural changes observed in the previously disturbed to undisturbed tundra profile between Slumps A and B (Figure 5).

The long-term GPS monitoring at Collinson Head shows that the retreat of the western part of the slump had decelerated or stopped before 2012, but that the eastern part of the slump had continued to retreat (Figure 8). In 2012, the slump was retreating in the northeast direction, which followed the direction of the steepest slope.

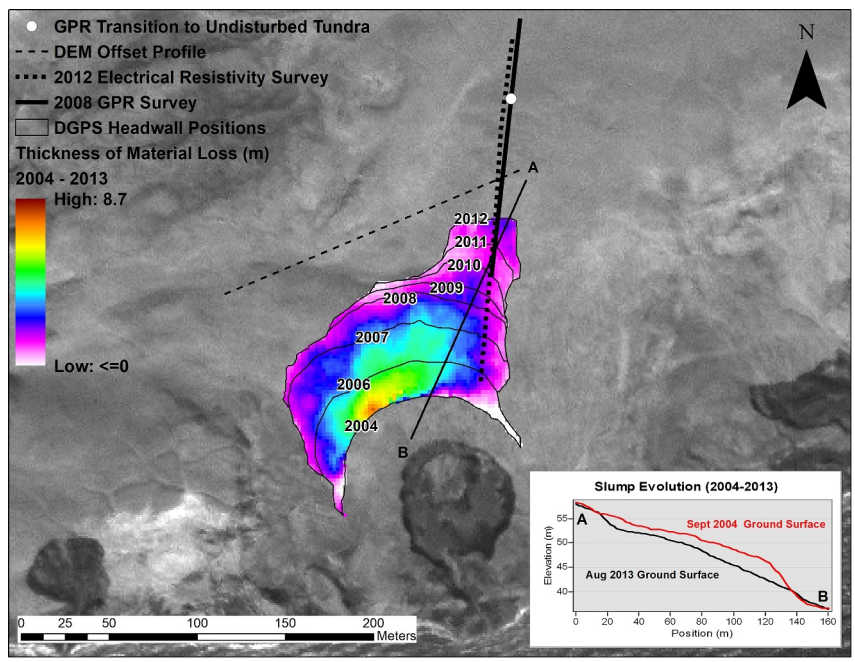

Figure 8. Monitored slump retreat and geophysical surveys at Collinson Head from 2004 to 2012 showed slump-induced lowering of the ground surface and the estimated amount of material loss. Toward the slump toe, sediment deposition raised the ground surface in some areas. The digital elevation models (DEM) offset profile is the transect line where the 2004 DEM and 2013 LiDAR Products were compared to correct for systematic offsets in the ground surface elevation differences. The structural transition revealed from the ground-penetrating radar indicates where a surface disturbance took place in the past. The background is a 2001 IKONOS satellite image. For position, see Figure 3.

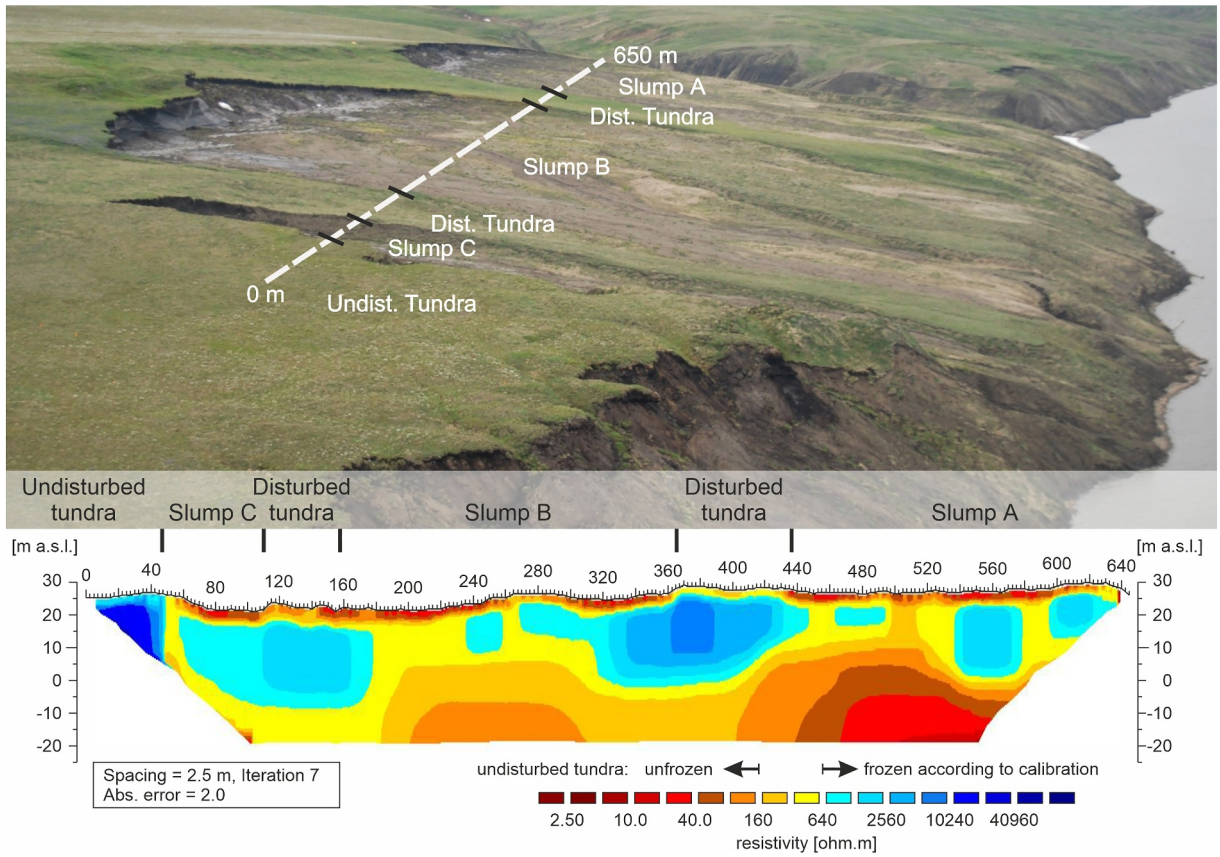

Figure 9. Electrical resistivity tomography profile crossing undisturbed tundra, previously disturbed tundra, and Slumps A, B, and C. Black lines represent mapped transitions along the transect. For positions, see Profile 3 in Figure 3. The calibration is according to Figure 4 and Section 4.1.

Toward the west, where the slump had decelerated or stopped, the headwall did not reach the steepest segment of the slope. From 2004 to 2008, the center of the slump retreated 60 m, with the maximum retreat being over 20 m between 2006 and 2007. Despite 40 m of retreat for the eastern portion of the slump between 2008 and 2012, the volumetric loss of material (including sediment and ground ice) steadily decreased since 2004. The difference between the 2004 and 2013 ground surfaces (thickness of material loss) decreased over time and the total material loss between the 2004 and 2012 headwall positions was $25.0 \pm 3.1 \times 10^3$ m^3. The error range was derived by using the standard deviation of the difference between the 2004 DEM and 2013 resampled DEM. The latter applies to slumps ABC as well.

4.3. Peak Polycyclic Reworking Stage (Slumps ABC)

To capture multiple cryostratigraphic settings, we carried out a 650 m-long ERT transect parallel to the headwall across Slumps A, B, and C (Figure 9). The survey started in undisturbed tundra, followed by the Slump C floor, previously disturbed tundra, the Slump B floor, previously disturbed tundra, and the Slump A floor. ERT generally showed that a surficial 0–5 m layer of unfrozen material (i.e., 0.04–0.32 kΩm, acc. to calibration in Figure 4) developed below the Slump A, B and C floors, in contrast to undisturbed tundra. Below this unit of unfrozen material, a 20 m thick layer (0–20 m a.s.l) with mostly frozen material was indicated by resistivities ranging from 0.6 to 10 kΩm below Slump A, B and C. Much higher resistivities (10–40 kΩm) occurred below undisturbed tundra. Interestingly, a layer with much lower resistivities (0.04–2.6 kΩm) was found below the sea level (0 m a.s.l.).

The long-term GPS monitoring showed that the middle of Slump A retreated 95 m between 2004 and 2013 (Figure 10), with the peak retreat being 15 m between 2006 and 2007. For Slump B, a coalescence of two thaw slumps occurred between 2004 and 2007. From 2006 to 2013, the retreat was 75 m in the center of the Slump B. The peak elevation difference between the 2004 and 2013 surfaces was 8.7 m in 2011. For Slump C, the headwall retreat was 110 m between 2004 and 2013, with the peak retreat being 18 m between 2012 and 2013. The material

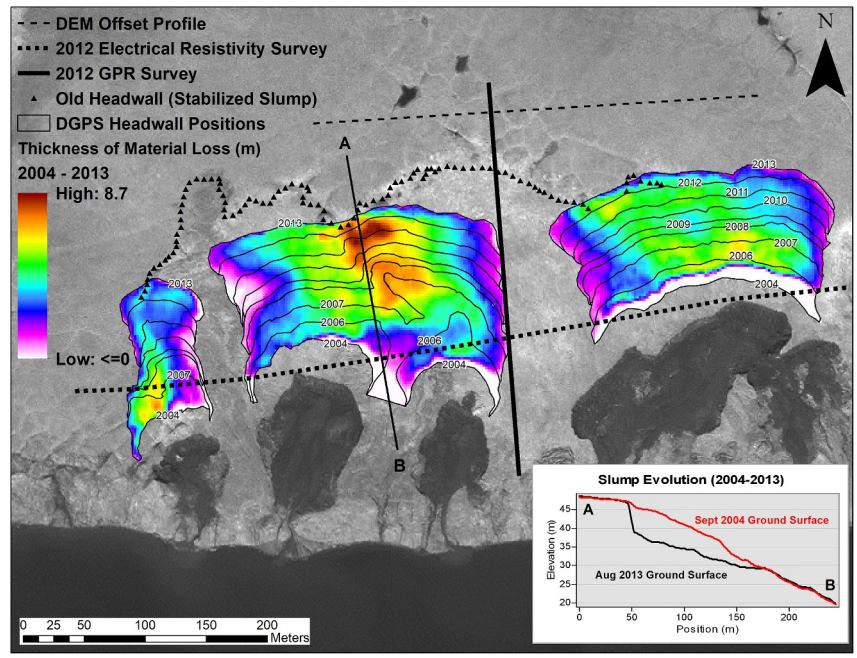

Figure 10. Slump evolution at Slumps A, B, and C from 2004 to 2013 with reference to the 2012 electrical resistivity tomography and ground-penetrating radar surveys. Headwall positions for 2005 are unavailable for all slumps and the headwall position for 2006 is absent for Slump C. We show slump-induced lowering of the ground surface and the estimated amount of material loss. Toward the slump toes, sediment deposition raised the ground surface in some areas. The digital elevation models (DEM) offset profile is the transect line where the 2004 DEM and 2013 LiDAR products were compared to correct for systematic offsets in the ground surface elevation differences. The background is a 2001 IKONOS satellite image. For positions, see Figure 3.

losses between 2004 and 2013 for slumps A, B, and C were $70.7 \pm 3.0 \times 10^3$ m^3, $101.7 \pm 4.0 \times 10^3$ m^3, and $18.3 \pm 1.0 \times 10^3$ m^3, respectively.

4.4. Super-Polycyclic Expansion (Slump D)

Slump D has been continuously active since the mid-1980s and represents the largest thaw slump on Herschel Island (De Krom & Pollard, 1989) and one of the largest in the Arctic. Here, we carried out a 500 m long ERT profile perpendicular to the headwall. The survey started at the shoreline and proceeded 50 m above the headwall (Figure 11). The survey intersected a shallow borehole approximately 280 m into the profile to verify the top of the ice-bonded permafrost. The mud flow thickness of 2 m overlying the ice-bearing permafrost matched with a low to high resistivity transition at about 1 kΩm. Below the permafrost core location, the resistivity increased with depth toward 10 kΩm. The permafrost core cut into a consistent structure we assumed to be recovered permafrost extending from 150 to 390 m on the survey line. We assume that (a) at positions which are not directly affected by mud deposition or gullying, the degradation of permafrost is incomplete and (b) under present climate conditions, the degraded permafrost would recover in a number of years. Just below the headwall at the mud pool, we observed a deep bulb of low resistivity with values approaching 10 Ωm. Below the headwall, on a solidly frozen slope that was partially still covered with snow, the resistivity exceeded 40 kΩm and above the headwall in previously disturbed terrain, the resistivity ranged from 1,280 to 10,000 Ωm. However, the most striking features were observed downslope of the permafrost coring location along a bifurcating creek that drains into the sea. From survey positions 150 m (the start of the gully) to 70 m, there was a lateral decrease in resistivity from 640 to 20 Ωm in the upper 10 m of the subsurface. Further downslope closer to the sea, the resistivities dipped below 20 Ωm.

For zoning, we considered that the transverse profile across slumps A, B, and C covered a more synchronous erosional/depositional stage than the Slump D longitudinal profile. Compared to Slumps A, B, and C, Slump D had a slightly thinner unfrozen surface zone of 2–4 m, only below the re-stabilized slump floor (150–270 m, 0.02–0.3 kΩm). The presumably frozen layer (1–20 kΩm) was visible below the re-stabilized slump floor, albeit only in

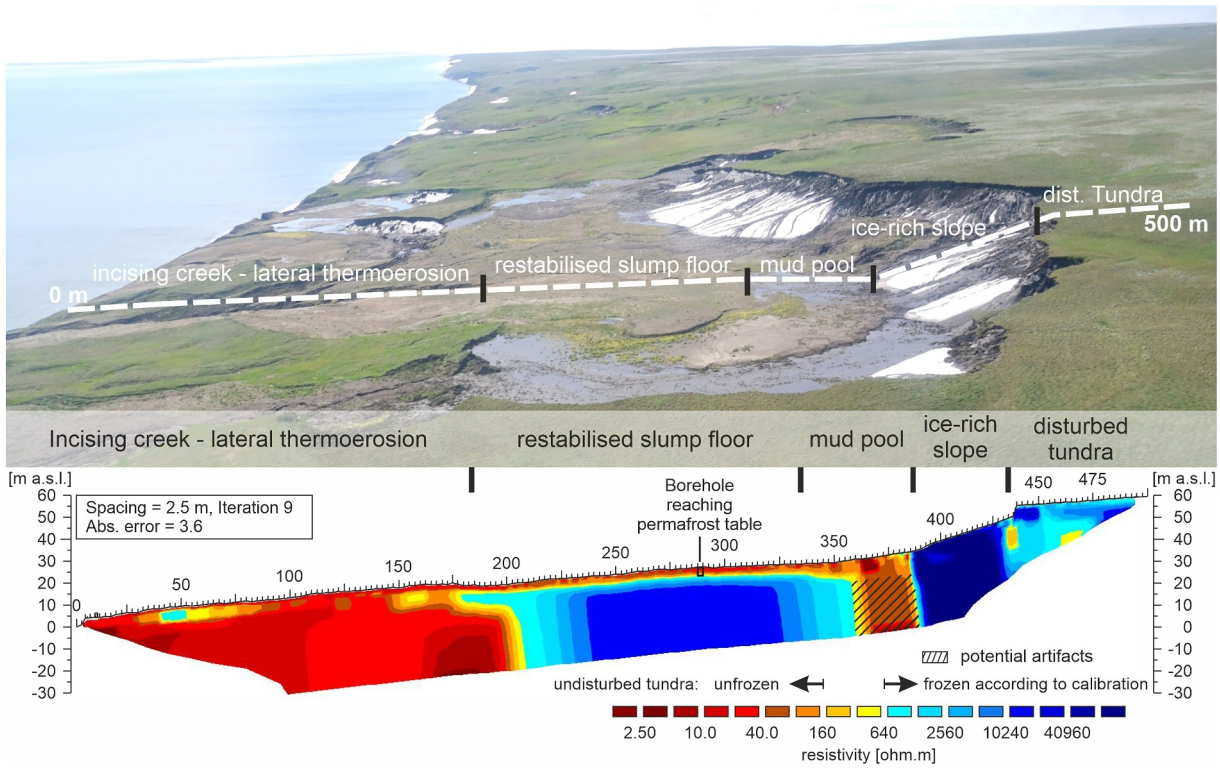

Figure 11. Aerial photograph and electrical resistivity tomography longitudinal profile perpendicular to the headwall of Slump D. For position, see Profile 5 in Figure 3. For potential artifacts, see Section 5.1. The calibration is according to Figure 4 and Section 4.1. However, from 0 to 200 m, the freezing transition is likely different due to higher salt content and sediment reworking.

its upper part (150–270 m inland from the shoreline). A low resistivity zone appeared below sea level and along the thermo-erosional gully within 120 m distance from the shoreline.

The thermal impact of the bifurcating creek was explored with seven 100 m lateral cross-sections across the creek (Figure 12). For the five northernmost cross-sections (55–135 m), the resistivity was less than 20 Ωm just below the creek and less than 40 Ωm down to a depth of 15 m below the ground surface, corresponding to water-saturated warm mud. However, for the two cross-sections closest to the sea (15–35 m), the minimum resistivity was less than 20 Ωm below sea level. For cross-section 15 m, the resistivity remained below 40 Ωm everywhere, even under the slump floor bounding the creek. For cross-section 35 m, the maximum resistivity on the west side of the creek ranged from 80 to 160 Ωm. For cross-section 55 m, the resistivity rapidly increased to 320 Ωm on the west side of the creek and then increased to 640 Ωm 30 m away from the creek. For cross-sections 75–115 m, the increase in resistivity west of the creek was more gradual. For example, a sharp increase in resistivity (80–640 Ωm) was observed 40 m west of the creek in cross-section 75 m. In the case of cross-section 115 m, the maximum resistivity west of the creek ranged from 80 to 160 Ωm within 5 m of the ground surface. West of the creek, we observed lateral sliding of slump material for cross-sections 75–115 m. Along cross-section 135 m, where no lateral sliding was observed, the resistivity sharply increased to 640 Ωm 10 m west of the creek, corresponding to the observed effect of thaw subsidence.

5. Discussion

5.1. Error Sources, Calibration, and Validation of ERT and GPR

The calibration of ERT tomographies showed that in undisturbed tundra (Figure 4), all permafrost probed depths correspond to the 0.6–1.0 kΩm resistivity range in the tomography. Validation in disturbed tundra was based on a borehole in Slump D directly beneath the electrode line, where thermal sensors indicate a permafrost depth of 2–2.5 m consistent with ERT (Figure 11). In GPR surveys, the transition to disturbed and undisturbed tundra is

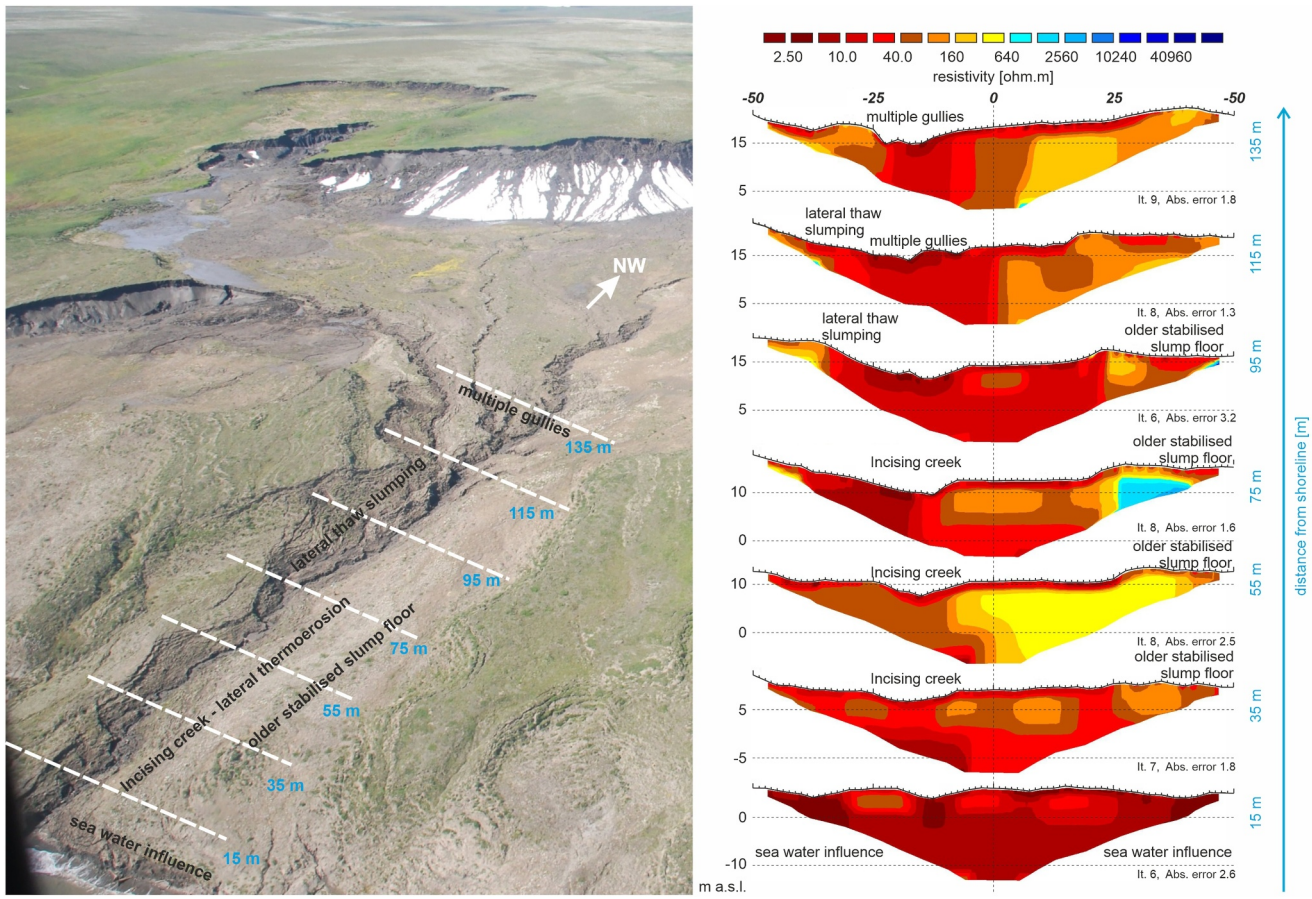

Figure 12. Aerial photograph and 3D analysis of seven parallel 100 m 2D electrical resistivity tomography images that investigate the thermal and mechanical imprint of incising creeks, thermoerosion, lateral thaw slumping, and seawater influence. Meters distance from the shoreline corresponds to the longitudinal profile of Slump D (Figure 11). Position see Profiles 6 in Figure 3. Calibration according to Figure 4 and Section 4.1, however, the freezing transition is likely different due to higher salt content and reworking.

indicated by the frequency of hyperbolic reflectors interpreted as massive ice features and complements the information provided by ERT calibration.

The applied Wenner-Array configuration is well-suited for the detection of horizontally layered resistivity contrasts but is less sensitive to sharp vertical resistivity structures. These vertical resistivity structures occur in Figures 6, 9, and 11 for instance at the transition from warm mud to vertical ice walls bridging two 2–3 magnitudes of resistivity. We have highlighted/camouflaged potential artifacts in the respective Figure 11. The apparent thaw depth beneath the mud pools in front of the headwall may be overestimated due to the high content of liquid water, which result in low resistivities and create a shadowing effect for underlying structures in the inversion process. Mud pools can lower resistivities in the permafrost by increasing the unfrozen water content; therefore, permafrost thaw is not a precondition for a high to low resistivity transition. Since RTS headwalls typically retreat several meters per year, mud pools lack sufficient time to create deep taliks.

5.2. Life Cycles of RTS

RTS can generate strong and deep thermal perturbations (>10 m) below slump floors, rendering them more susceptible to polycyclic activity. Furthermore, the permafrost is mechanically disturbed, particularly in the near-surface sediment (2–3 m), where thick mud flow deposits accumulate above the frozen ground. The scale and magnitude of disturbance is related to the polycyclic slump stage (dormant, initial, peak or super-polycyclic) as well as the time elapsed since the previous disturbance.

At Collinson Head, the thermal perturbation beneath the active slump floor is minor compared to Slumps ABC and Slump D. The shallow mud pool below the 2012 headwall is likely responsible for the low resistivity bulb that penetrates several meters below the ground surface (Figure 6). Given the high clay content in the sediment, the resistivity of frozen material for warm permafrost can be on the order of 10^2 Ωm (Fortier et al., 1994), while laboratory experiments show that the frozen resistivity of saline marine sediments approaches values as low as 10 Ωm (Overduin et al., 2012). Downslope of the headwall, the resistivity of the permafrost beneath the mud flow deposits is characteristic of ice-bonded permafrost (>10 kΩm), but still less than values observed in undisturbed tundra (40 kΩm). We have made extensive measurements on undisturbed tundra to find a consistent value range of ≥40 kΩm (e.g., in Figure 4 along the entire transect). This indicates a warming of the remaining permafrost after slump activity. Although the mean annual ground surface temperature is estimated at −8°C (Burn & Zhang, 2009), the removal of the organic layer can cause a 3–4°C increase in the mean annual ground surface temperature as shown by Burn (2000) in Mayo, Yukon. For marine clays, this may result in unfrozen water content changes and thus resistivity changes (Anderson et al., 1973). Surprisingly, the resistivity upslope of the headwall is also lower compared with undisturbed permafrost. The gradual increase in resistivity from 2.5 to 40 kΩm at 100–200 m could represent the transition from previously disturbed (i.e., a former slump floor) to undisturbed permafrost. While the surface expression—a densely vegetated scarp indicating a former headwall—is absent, the structural effects of past disturbance remain. In the GPR profile (Figure 7), the shift from parallel continuous reflections to multiple hyperbolic reflections suggests a transition from mud flow deposits from previous mass movements to numerous ice wedges in undisturbed permafrost (Moorman et al., 2003). As noted by De Krom (1990), there are many active layer detachments in the area. The RTS current trajectory follows the direction of the steepest slope, but the long-term GPS monitoring shows that in the present phase the slump will not overtake the previous headwall. Slump activity will most likely stop.

At Slumps ABC, the thermal perturbation of permafrost is noticeably greater and reaches much deeper (Figure 9). Beneath the floors of Slumps A and B, the electrical resistivity of permafrost varied between 0.6 and 26 kΩm. In addition to organic material removal, permafrost warming is controlled by massive meltwater discharge and mud flows. Between 2004 and 2013, the total material loss was three to four times greater for Slump A and Slump B compared to Collinson Head. Additionally, the permafrost resistivity was an order of magnitude less beneath the floors of slumps A and B compared to Collinson Head, and two orders of magnitude less than in undisturbed tundra. The chimney-like structure observed 500 m into the profile could possibly be the result of a gully where permafrost warming is accelerated by the heat transfer of flowing water (de Grandpré et al., 2012). The most prominent feature, however, is the sharp decrease in resistivity at sea level. The low resistivity layer at or below sea level suggests that the seawater has an effect on the slump several decameters inland, which is not yet fully understood. This low resistivity layer at or below sea level may partially be attributed to the thermal influence of the sea and not only to seawater intrusion. Kasprzak et al. (2017) showed that the lateral heat flow and seawater intrusion affected the position of basal permafrost along the coast of Spitsbergen several decameters inland. On Herschel Island, however, the permafrost thickness can reach 300 m (Smith & Burgess, 2000). As demonstrated by multiple subsea permafrost studies, salt diffusion is a slow process and typically slower than heat diffusion at degrading ice-rich permafrost (Angelopoulos, Overduin, Miesner, et al., 2020; Angelopoulos, Overduin, Westermann, et al., 2020; Harrison & Osterkamp, 1978; Razumov et al., 2014). Coupled heat and salt diffusion models reveal that it would take over 1,000 years to thaw 6 m of cold ice-rich permafrost from the top down under Arctic seawater characterized by mean annual cryotic seabed temperatures (Angelopoulos et al., 2019). The lateral diffusion of salt is expected to be much slower than the coastal retreat of Herschel Island. We suspect that seawater intrusion can penetrate already unfrozen sediment caused by the deep warming and thawing associated with the removal of vegetation, meltwater discharge and mud flow from the headwall. Seawater intrusion could degrade ice-rich permafrost at or near sea level, leading to subsidence. This subsidence, visible at the ground surface, could lead to ground ice exposure and the next phase of polycyclic slumping. Subsidence caused by deep permafrost thaw has been shown by Stephani et al. (2015), who explored the development of groundwater flow paths between active and reclamation mine pits in cold and continuous permafrost in Alaska. Talik formation and surface subsidence have also triggered new slump formation around Parsons Lake (Kokelj et al., 2009). Since the low resistivity layer below sea level was not observed at Collinson Head or Slump C (both smaller slumps), the intrusion of seawater seems unlikely without a sufficient initial thermal perturbation caused by gullying, meltwater discharge, and mud flows. Interestingly, the low resistivity layer below sea level is still present beneath slumps A and B where a previous

thaw slump might have existed. Vegetation succession studies show that this area has been recovering from disturbance for about 250 years (Cray & Pollard, 2015). While the permafrost above sea level has recovered to resistivities as high as 20 kΩm, the resistivity below sea level is still below 1.3 kΩm. Although the seawater-affected layer can still be cryotic, the presence of salts can reduce the resistivity of ice-bearing saline material (Overduin et al., 2012). Further permafrost warming at the ground surface can make ice-bearing saline sediment susceptible to cryopeg formation. The formation of cryopegs could also lead to subsidence and trigger polycyclic thermokarst.

At Slump D (Figure 11), within 120 m inland from the shoreline, the resistivities are less than 20 Ωm everywhere in the model domain below sea level. A possible landward intrusion of seawater would be facilitated by the deep thermal influence of the bifurcating creek. However, it is highly unlikely that seawater intrusion would occur faster than the coastal erosion on Herschel Island, where coastal retreat rates of 0.6 m/a are common (Lantuit et al., 2012). Evaluating these low resistivities, a combination of a marine sediment layer, which is documented for Herschel Island (Pollard, 1990; Wetterich et al., 2023) and the presence of unfrozen water due to the gully incision and permafrost warming should be considered as an explanation. Nevertheless, seawater intrusion at the toe of the slump might occur several meters inland and the corresponding destabilization could lead to slump initiation. Although the resistivities are less than 20 Ωm, it is highly unlikely that there is unfrozen sediment ∼30 m thick nearshore. In addition to seawater intrusion, glacial thrusting (at the time of the island formation) might have created pockets of saline permafrost. Therefore, the sharp lateral resistivity transition we observe could also be representative of a saline permafrost to buried glacial ice boundary. To determine whether there is a masking effect by highly saline and thawed surface sediment as demonstrated by Arboleda-Zapata et al. (2022) or if there is a geological structure with highly saline permafrost, additional sensitivity analyses and further field data such as boreholes with temperature loggers would be ideal. In addition to heat transfer from flowing water in the creek, the gullies may act as snow traps, thus inhibiting cooling in winter. Furthermore, the thermal impact of lateral sliding is evident from cross-sections showing lower resistivity values west of the bifurcating creek (Figure 12). Above the intersection of the two smaller creeks, there is a sharp lateral increase in resistivity. Here, the slump floor has already started to re-stabilize and revegetate. The underlying resistivity of permafrost is over 10 kΩm, which is similar to permafrost below the slump floor of Collinson Head. Thus, in areas where seawater intrusion, gullies, and increased meltwater discharge are not a factor, the change in resistivity caused by permafrost warming through slump retreat and the removal of an organic cover ranges from 40 to 10 kΩm. Below the headwall, where there is a massive decameter-long and several meters wide mud pool, the thermal disturbance is much deeper compared to Collinson Head. While a short-term talik is possible, a newly formed talik would likely refreeze following continued headwall retreat and the displacement of the mud pool. Despite the fact that Figure 11 shows low resistivities beneath the headwall down to a depth of 30 m below the surface, this is an exaggerating artifact of the robust inversion induced by the sharp resistivity transition between the mud pool and the very ice-rich solidly frozen slope. Here, the modeled resistivities emphasize lateral shifts in the subsurface structure.

With rising global permafrost temperatures (Biskaborn et al., 2019) and accelerated thaw slump development in the High Arctic (Lewkowicz & Way, 2019; Ward Jones et al., 2019) and Herschel Island (Lantuit & Pollard, 2008), our results suggest that polycyclic slump behavior may increase. Warming summers may increase meltwater discharge from slumps and enhance the thermal disturbance from gully erosion and mud flows. This in turn may promote seawater intrusion at the toe of thaw slumps, leading to further permafrost degradation, subsidence, and polycyclic slumping. For salt-induced thixotropy, the mechanical impacts of the reworked material from mud flows could persist much longer than thermal recovery times. With increasing slump activity from warming permafrost, the coalescence of small slumps may become more probable. Thus, we may see an increase in larger slumps, which are more susceptible to polycyclic thermokarst.

We suggest three main processes that determine the polycyclicity of RTS (Figure 13). First, deep-reaching thermal perturbations are caused by the energetics of mud transport and deposition. These determine the spatial scale of polycyclicity, where creek incision and resulting lateral sliding cause decameter large disturbances and the heat intake in mud pools leads to thaw bulbs in front of the head scarp (Slump D). The thermal recovery of the disturbed permafrost body might take decades to centuries and presumably determines the time scale of polycyclicity, exemplified by the thawed material under the 300-year old MRTS ABC. Second, coastal influence might not be limited to coastal erosion but might also affect toe stability due to saltwater intrusion,

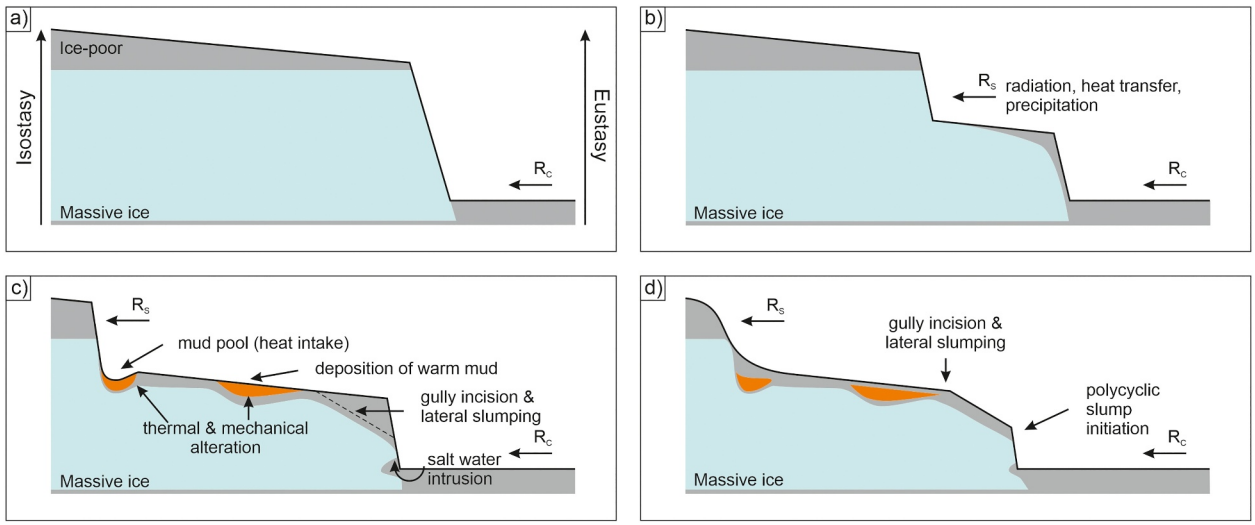

Figure 13. Schematic representation of a cycle of slump initiation, stabilization and polycyclic re-initiation in an idealized coastal setting. (a) Initial state, (b) Initial slump formation, (c) peak stage and (d) polycyclic slump initiation. R_S = rate of headwall retreat; R_C = rate of coastal retreat, based on Lantuit et al. (2012) and modified with findings of this article.

which contributes to ground-ice melting and permafrost thaw near the shoreline. Very low resistivities below sea level exist several decameters inland under many RTS, and these features are not found under stable tundra. Third, deep-reaching effects such as overconsolidation, thixotropy, and salt-bonding may result in mechanical predisposition for polycyclic RTS behavior, but these impacts need to be studied in more detail. The initial thawing of salt-rich fine-grained sediments will destroy salt bonds between clay and silt particles and can have thixotropic effects (Perret et al., 1996). It is also possible that salt effects play an active role in the destabilization of RTS near the shoreline by impacting mechanical stability.

5.3. Synthetic Classification of MRTS Polycyclic Development Stages Characterized by Geomorphological Processes, Vegetation, ERT, and GPR Structures

In this study, we developed a geophysical framework to distinguish the stages of polycyclic reworking. We postulate that development stages starting from a dormant stage to an initial and peak polycyclic reworking stage and possibly a super polycyclic expansion stage can be deciphered by their distinctive ERT and GPR signatures (Table 3). In this table, we do not claim that all MRTS will automatically evolve from one stage to the next. We rather aim at providing a classification scheme to cluster MRTS which are in a similar evolution stage and thus exhibit similar controls and evolution trajectories. ERT and GPR provide unprecedented insights into the depth, duration, and subsurface distribution of thermal degradation inside MRTS. This technical advance could help to anticipate the susceptibility to future polycyclicity and perhaps also limit the maximum extent of rapidly evolving MRTS in the foreseeable future.

6. Conclusions

- We investigated RTS in dormant, initial, peak and super-polycyclic stages and compared them with sites with proven historical RTS activity since 300 years BP and with undisturbed sites. The electrical resistivity and GPR surveys indicate spatial and temporal thaw slump dynamics in all development stages.
- The resistivity surveys show an impact of seawater and associated warming at the toe of the slumps extending several meters inland. This could initiate a destabilization starting from the slump toe and trigger polycyclic MRTS.
- In the super-polycyclic stage, gully incisions transport massive amounts of sediment and organic matter to the shoreline and act as a heat source affecting the underlying permafrost. In addition, they often expose the underlying massive ground ice and act as a point of slump re-initiation.
- We can show that both the accumulation of liquid water, mud pools and mud flows, as well as the incision of gullies have a decadal impact on permafrost temperatures and the mechanics of thaw slumps.

Table 3
Summarizing Table of Mega Retrogressive Thaw Slump Polycyclic Development and Indicative Geomorphological and Geophysical Electrical Resistivity Tomography and Ground-Penetrating Radar Signatures

	Typical Active Slump Age [a]	Process and Development Stage (Table 1)	Example	ERT Signature (Table 2)	GPR Signature
0a. Undisturbed tundra			Slump D	Ice wedges and massive ice bodies with >40 kΩm	Near surface hyperbolic reflections indicating ice wedges
0b. Dormant stage			Collinson Head	Refrozen mixed sediments 10–40 kΩm	Absence of near surface hyperbolic reflections representative of ice wedges
1. Initial polycyclic reworking stage	10^0–10^1	• Initial mud pool development • Headwall 10^0–10^1 m • Length/Width 10^1 m • Single lobe structure	Collinson Head	Small mud pools and mud flow deposits; unfrozen layer a few meters deep	
2. Peak Polycyclic reworking stage	10^1–10^2	• Massive mud pool • Headwall 5–30 m • Length/Width 10^1–10^2 m • Multiple lobe structure	Slumps A, B, C	Initial formation of thermoerosion, gullying and refreezing zones (commonly 10^2–10^3 Ωm)	
3. Super-polycyclic expansion	10^1–10^2+	• Coalescence of multiple peak polycyclic stage slumps • Widespread expansion beyond old headwall into undisturbed tundra • Intense meltwater discharge from the headwall and gullying on the slump floor	Slump D; C & A (in transition from stage 2–3)	Massive differentiation of slump floors into thermoerosion, gullying and refreezing zones (extensive zones 10^1–10^2 Ωm)	

- Deep-reaching thermal perturbations, triggered by bimodal flows and shoreline activity, persist for hundreds of years and are clearly distinguishable from undisturbed tundra slopes.
- Here we show how 20–30 m deep geophysical data and associated field surveys can help create a better understanding of the temporal and spatial patterns, as well as memory effects of MRTS and their response to atmospheric and marine forcing.

Data Availability Statement

The electrical resistivity data and its metadata are available in the online data publication (Krautblatter & Angelopoulos, 2024).

Acknowledgments
We wish to express our thanks to the Yukon Territorial Government and the Yukon Parks (Herschel Island Qikiqtaruk Territorial Park). The authors acknowledge the support of the Aurora Research Institute (ARI, Inuvik) for the field component. This publication is part of the NUNATARYUK project that received funding from the European Union's Horizon 2020 research and innovation program under grant agreement No. 773421. S. Eppinger was financed by the German Federal Environmental Foundation (DBU 20018/563). W. Pollard received funding from the National Sciences and Engineering Research Council of Canada (NSERC), the Polar Continental Shelf Project (PCSP), and the Northern Scientific Training Program (NSTP). We thank Torsten Sachs (GFZ) for providing LiDAR data. We also thank Dr. Paul Overduin for providing comments on the manuscript before submission. Heather Cray, Jared Simpson, Dave Fox, and Ute Kuschel enormously supported the often difficult fieldwork. We thank J.M. Reynolds and two anonymous reviewers for their comments that greatly helped to improve this manuscript. Open Access funding enabled and organized by Projekt DEAL.

References

Alumbaugh, D. L., & Newman, G. A. (2000). Image appraisal for 2-D and 3-D electromagnetic inversion. *Geophysics*, *65*(5), 1455–1467. https://doi.org/10.1190/1.1444834

Anderson, D. M., Tice, A. R., & McKim, H. L. (1973). The unfrozen water and the apparent specific heat capacity of frozen soils. In *Paper presented at 2nd International Conference on Permafrost, Yakutsk, USSR*.

Angelopoulos, M., Overduin, P. P., Jenrich, M., Nitze, I., Günther, F., Strauss, J., et al. (2021). Onshore thermokarst primes subsea permafrost degradation. *Geophysical Research Letters*, *48*(20), e2021GL093881. https://doi.org/10.1029/2021GL093881

Angelopoulos, M., Overduin, P. P., Miesner, F., Grigoriev, M. N., & Vasiliev, A. A. (2020). Recent advances in the study of Arctic submarine permafrost. *Permafrost and Periglacial Processes*, *31*(3), 442–453. https://doi.org/10.1002/ppp.2061

Angelopoulos, M., Overduin, P. P., Westermann, S., Tronicke, J., Strauss, J., Schirrmeister, L., et al. (2020). Thermokarst lake to lagoon transitions in eastern Siberia: Do submerged taliks refreeze? *Journal of Geophysical Research: Earth Surface*, *125*(10), e2019JF005424. https://doi.org/10.1029/2019JF005424

Angelopoulos, M., Westermann, S., Overduin, P. P., Faguet, A., Olenchenko, V., Grosse, G., & Grigoriev, M. N. (2019). Heat and salt flow in subsea permafrost modeled with CryoGRID2. *Journal of Geophysical Research: Earth Surface*, *124*(4), 920–937. https://doi.org/10.1029/2018JF004823

Arboleda-Zapata, M., Angelopoulos, M., Overduin, P. P., Grosse, G., Jones, B. M., & Tronicke, J. (2022). Exploring the capabilities of electrical resistivity tomography to study subsea permafrost. *The Cryosphere*, *16*(10), 4423–4445. https://doi.org/10.5194/tc-16-4423-2022

Are, F. E., Grigoriev, M. N., Hubberten, H. W., & Rachold, V. (2005). Using thermoterrace dimensions to calculate the coastal erosion rate. *Geo-Marine Letters*, *25*(2–3), 121–126. https://doi.org/10.1007/s00367-004-0193-y

Biskaborn, B. K., Smith, S. L., Noetzli, J., Matthes, H., Vieira, G., Streletskiy, D. A., et al. (2019). Permafrost is warming at a global scale. *Nature Communications*, *10*(1), 264. https://doi.org/10.1038/s41467-018-08240-4

Bouchard, M. (1974). *Géologie des dépôts meubles de l'île Herschel, Territoire du Yukon* (M.Sc. Thesis thesis). Université de Montréal.

Burn, C. R. (2000). The thermal regime of a retrogressive thaw slump near Mayo, Yukon Territory. *Canadian Journal of Earth Sciences*, *37*(7), 967–981. https://doi.org/10.1139/e00-017

Burn, C. R., & Zhang, Y. (2009). Permafrost and climate change at Herschel Island (Qikiqtaruq), Yukon Territory, Canada. *Journal of Geophysical Research*, *114*(F2), F02001. https://doi.org/10.1029/2008jf001087

Cray, H. A., & Pollard, W. H. (2015). Vegetation recovery patterns following permafrost disturbance in a Low Arctic setting: Case study of Herschel Island, Yukon, Canada. *Arctic, Antarctic, and Alpine Research*, *47*(1), 99–113. https://doi.org/10.1657/AAAR0013-076

de Grandpré, I., Fortier, D., & Stephani, E. (2012). Degradation of permafrost beneath a road embankment enhanced by heat advected in groundwater. *Canadian Journal of Earth Sciences*, *49*(8), 953–962. https://doi.org/10.1139/E2012-018

De Krom, V. D. (1990). *A geomorphic investigation of retrogressive thaw slumps and active layer slides on Herschel Island, Yukon* (M.Sc. Thesis). McGill University.

De Krom, V. D., & Pollard, W. H. (1989). The occurrence of retrogressive thaw slumps on Herschel Island, Yukon Territory. *Musk-Ox*, *37*, 1–7.

Fortier, R., Allard, M., & Seguin, M. K. (1994). Effect of physical properties of frozen ground on electrical resistivity logging. *Cold Regions Science and Technology*, *22*(4), 361–384. https://doi.org/10.1016/0165-232X(94)90021-3

Fox, D. (2012). *Observations of massive ground ice Herschel Island, Yukon Territory*. Masters thesis. McGill University.

French, H. M. (1998). An appraisal of cryostratigraphy in north-west Arctic Canada. *Permafrost and Periglacial Processes*, *9*(4), 297–312. https://doi.org/10.1002/(SICI)1099-1530(199810/12)9:4<297::AID-PPP296>3.0.CO;2-B

Fritz, M., Wetterich, S., Meyer, H., Schirrmeister, L., Lantuit, H., & Pollard, W. H. (2011). Origin and characteristics of massive ground ice on Herschel Island (western Canadian Arctic) as revealed by stable water isotope and Hydrochemical signatures. *Permafrost and Periglacial Processes*, *22*(1), 26–38. https://doi.org/10.1002/ppp.714

Fritz, M., Wetterich, S., Schirrmeister, L., Meyer, H., Lantuit, H., Preusser, F., & Pollard, W. H. (2012). Eastern Beringia and beyond: Late Wisconsinan and Holocene landscape dynamics along the Yukon Coastal Plain, Canada. *Palaeogeography, Palaeoclimatology, Palaeoecology*, *319–320*, 28–45. https://doi.org/10.1016/j.palaeo.2011.12.015

Fritz, M., Wolter, J., Rudaya, N., Palagushkina, O., Nazarova, L., Obu, J., et al. (2016). Holocene ice-wedge polygon development in northern Yukon permafrost peatlands (Canada). *Quaternary Science Reviews*, *147*, 279–297. https://doi.org/10.1016/j.quascirev.2016.02.008

Harrison, W. D., & Osterkamp, T. E. (1978). Heat and mass transport processes in subsea permafrost 1. An analysis of molecular diffusion and its consequences. *Journal of Geophysical Research*, *83*(C9), 4707–4712. https://doi.org/10.1029/JC083iC09p04707

Jones, B. M., Stoker, J. M., Gibbs, A. E., Grosse, G., Romanovsky, V. E., Douglas, T. A., et al. (2013). Quantifying landscape change in an arctic coastal lowland using repeat airborne LiDAR. *Environmental Research Letters*, *8*(4), 045025. https://doi.org/10.1088/1748-9326/8/4/045025

Kasprzak, M., Strzelecki, M. C., Traczyk, A., Kondracka, M., Lim, M., & Migała, K. (2017). On the potential for a bottom active layer below coastal permafrost: The impact of seawater on permafrost degradation imaged by electrical resistivity tomography (Hornsund, SW Spitsbergen). *Geomorphology*, *293*, 347–359. https://doi.org/10.1016/j.geomorph.2016.06.013

Kizyakov, A. I., Wetterich, S., Günther, F., Opel, T., Jongejans, L. L., Courtin, J., et al. (2023). Landforms and degradation pattern of the Batagay thaw slump, Northeastern Siberia. *Geomorphology*, *420*, 108501. https://doi.org/10.1016/j.geomorph.2022.108501

Kizyakov, A. I., Zimin, M. V., Leibman, M. O., & Pravikova, N. V. (2013). Monitoring of the rate of thermal denudation and thermal abrasion on the western coast of Kolguyev Island, using high resolution satellite images. *Earth's Cryosphere*, *17*(4), 36–47.

Kokelj, S. V., Kokoszka, J., van der Sluijs, J., Rudy, A. C. A., Tunnicliffe, J., Shakil, S., et al. (2021). Thaw-driven mass wasting couples slopes with downstream systems, and effects propagate through Arctic drainage networks. *The Cryosphere*, *15*(7), 3059–3081. https://doi.org/10.5194/tc-15-3059-2021

Kokelj, S. V., Lacelle, D., Lantz, T. C., Tunnicliffe, J., Malone, L., Clark, I. D., & Chin, K. S. (2013). Thawing of massive ground ice in mega slumps drives increases in stream sediment and solute flux across a range of watershed scales. *Journal of Geophysical Research: Earth Surface*, *118*(2), 681–692. https://doi.org/10.1002/jgrf.20063

Kokelj, S. V., Lantz, T. C., Kanigan, J., Smith, S. L., & Coutts, R. (2009). Origin and polycyclic behaviour of tundra thaw slumps, Mackenzie Delta region, Northwest Territories, Canada. *Permafrost and Periglacial Processes*, *20*(2), 173–184. https://doi.org/10.1002/ppp.642

Kokelj, S. V., Lantz, T. C., Tunnicliffe, J., Segal, R., & Lacelle, D. (2017). Climate-driven thaw of permafrost preserved glacial landscapes, northwestern Canada. *Geology*, *45*(4), 371–374. https://doi.org/10.1130/G38626.1

Kokelj, S. V., Smith, C. A. S., & Burn, C. R. (2002). Physical and chemical characteristics of the active layer and permafrost, Herschel Island, western Arctic Coast, Canada. *Permafrost and Periglacial Processes*, *13*(2), 171–185. https://doi.org/10.1002/ppp.417

Kokelj, S. V., Tunnicliffe, J., Lacelle, D., Lantz, T. C., Chin, K. S., & Fraser, R. (2015). Increased precipitation drives mega slump development and destabilization of ice-rich permafrost terrain, northwestern Canada. *Global and Planetary Change*, *129*, 56–68. https://doi.org/10.1016/j.gloplacha.2015.02.008

Krautblatter, M. (2010). Patterns of multiannual aggradation of permafrost in rock walls with and without hydraulic interconnectivity (Steintälli, Valley of Zermatt, Swiss Alps). In *Lecture Notes in Earth Sciences* (pp. 199–219). https://doi.org/10.1007/978-3-540-75761-0_13

Krautblatter, M., & Angelopoulos, M. (2024). ERT datasets of the article "Life cycles and polycyclicity of mega retrogressive thaw slumps in Arctic permafrost revealed by 2D/3D geophysical and long-term retreat monitoring" (1.0) [Dataset]. *Technical University of Munich*. https://doi.org/10.14459/2024MP1739720.001

Kunz, J., Ullmann, T., Kneisel, C., & Baumhauer, R. (2023). Three-dimensional subsurface architecture and its influence on the spatiotemporal development of a retrogressive thaw slump in the Richardson Mountains, Northwest Territories, Canada. *Arctic, Antarctic and Alpine Research*, *55*(1), 19. https://doi.org/10.1080/15230430.2023.2167358

Lacelle, D., Brooker, A., Fraser, R., & Kokelj, S. (2015). Distribution and growth of thaw slumps in the Richardson Mountains–Peel Plateau region, northwestern Canada. *Geomorphology*, *235*, 40–51. https://doi.org/10.1016/j.geomorph.2015.01.0241

Lantuit, H., & Pollard, W. H. (2005). Temporal stereophotogrammetric analysis of retrogressive thaw slumps on Herschel Island, Yukon Territory. *Natural Hazards and Earth System Science*, *5*(3), 413–423. https://doi.org/10.5194/nhess-5-413-2005

Lantuit, H., & Pollard, W. H. (2008). Fifty years of coastal erosion and retrogressive thaw slump activity on Herschel Island, southern Beaufort Sea, Yukon Territory, Canada. *Geomorphology*, *95*(1–2), 84–102. https://doi.org/10.1016/j.geomorph.2006.07.040

Lantuit, H., Pollard, W. H., Couture, N., Fritz, M., Schirrmeister, L., Meyer, H., & Hubberten, H. W. (2012). Modern and late Holocene retrogressive thaw slump activity on the Yukon coastal plain and Herschel Island, Yukon Territory, Canada. *Permafrost and Periglacial Processes*, *23*(1), 39–51. https://doi.org/10.1002/ppp.1731

Lantuit, H., Rachold, V., Pollard, W. H., Steenhuisen, F., Odegard, R., & Hubberten, H. W. (2009). Towards a calculation of organic carbon release from erosion of Arctic coasts using non-fractal coastline datasets. *Marine Geology*, *257*(1–4), 1–10. https://doi.org/10.1016/j.margeo.2008.10.004

Lantz, T. C., & Kokelj, S. V. (2008). Increasing rates of retrogressive thaw slump activity in the Mackenzie Delta region, NWT, Canada. *Geophysical Research Letters*, *35*(6), L06502. https://doi.org/10.1029/2007gl032433

Leibman, M. O., Gubarkov, A., Khomutov, A., Kizyakov, A. I., & Vanshtein, B. (2008). Coastal processes at the tabular-ground-ice-bearing area, Yugorsky Peninsula, Russia. In *Paper presented at 9th International Conference on Permafrost, University of Alaska Fairbanks, June 29–July 3 2008*.

Lewkowicz, A. G. (1987a). Headwall retreat of ground-ice slumps, Banks Island, Northwest Territories. *Canadian Journal of Earth Sciences*, *24*(6), 1077–1085. https://doi.org/10.1139/e87-105

Lewkowicz, A. G. (1987b). Nature and importance of thermo-karst processes, Sand Hills moraine, Banks Island, Canada. *Geografiska Annaler, Series A*, *69 A*(2), 321–327. https://doi.org/10.1080/04353676.1987.11880218

Lewkowicz, A. G. (1988). Slope processes. In M. J. Clark (Ed.), *Advances in periglacial geomorphology* (pp. 325–368). John Wiley and Sons.

Lewkowicz, A. G., & Way, R. G. (2019). Extremes of summer climate trigger thousands of thermokarst landslides in a High Arctic environment. *Nature Communications*, *10*(1), 1329. https://doi.org/10.1038/s41467-019-09314-7

Littlefair, C. A., Tank, S. E., & Kokelj, S. V. (2017). Retrogressive thaw slumps temper dissolved organic carbon delivery to streams of the Peel Plateau, NWT, Canada. *Biogeosciences*, *14*(23), 5487–5505. https://doi.org/10.5194/bg-14-5487-2017

Mackay, J. R. (1959). Glacier ice-thrust features of the Yukon coast. *Geographical Bulletin*, *13*, 5–21.

Mackay, J. R. (1966). Segregated epigenetic ice and failures in permafrost, Mackenzie Delta area, N.W.T. *Geographical Bulletin*, *8*, 59–80.

Moorman, B. J., Robinson, S. D., & Burgess, M. M. (2003). Imaging periglacial conditions with ground-penetrating radar. *Permafrost and Periglacial Processes*, *14*(4), 319–329. https://doi.org/10.1002/ppp.463

Morgenstern, N. R., & Nixon, J. F. (1971). One-dimensional consolidation of thawing soils. *Canadian Geotechnical Journal*, *8*(4), 558–565. https://doi.org/10.1139/t71-057

Murton, J. B., Opel, T., Wetterich, S., Ashastina, K., Savvinov, G., Danilov, P. P., & Boeskorov, V. (2023). Batagay megaslump: A review of the permafrost deposits, Quaternary environmental history, and recent development. *Permafrost and Periglacial Processes*, *34*(3), 399–416. https://doi.org/10.1002/ppp.2194

Obu, J., Lantuit, H., Fritz, M., Grosse, G., Günther, F., Sachs, T., & Helm, V. (2016). LiDAR elevation data of Yukon Coast and Herschel Island in 2012 and 2013. *Geomorphology*, *293*, 331–346. https://doi.org/10.1594/PANGAEA.859046

Obu, J., Lantuit, H., Fritz, M., Pollard, W. H., Sachs, T., & Günther, F. (2016). Relation between planimetric and volumetric measurements of permafrost coast erosion: A case study from Herschel Island, western Canadian Arctic. *Polar Research*, *35*(2016), 30313. https://doi.org/10.3402/polar.v35.30313

Obu, J., Lantuit, H., Grosse, G., Günther, F., Sachs, T., Helm, V., & Fritz, M. (2017). Coastal erosion and mass wasting along the Canadian Beaufort Sea based on annual airborne LiDAR elevation data. *Geomorphology*, *293*, 331–346. https://doi.org/10.1016/j.geomorph.2016.02.014

Olefeldt, D., Goswami, S., Grosse, G., Hayes, D., Hugelius, G., Kuhry, P., et al. (2016). Circumpolar distribution and carbon storage of thermokarst landscapes. *Nature Communications*, *7*(1), 13043. https://doi.org/10.1038/ncomms13043

Opel, T., Murton, J. B., Wetterich, S., Meyer, H., Ashastina, K., Günther, F., et al. (2019). Past climate and continentality inferred from ice wedges at Batagay megaslump in the Northern Hemisphere's most continental region, Yana Highlands, interior Yakutia. *Climate of the Past*, *15*(4), 1443–1461. https://doi.org/10.5194/cp-15-1443-2019

Overduin, P. P., Westermann, S., Yoshikawa, K., Haberlau, T., Romanovsky, V., & Wetterich, S. (2012). Geoelectric observations of the degradation of nearshore submarine permafrost at Barrow (Alaskan Beaufort Sea). *Journal of Geophysical Research*, *117*(2), F02004. https://doi.org/10.1029/2011JF002088

Perret, D., Locat, J., & Martignoni, P. (1996). Thixotropic behavior during shear of a fine-grained mud from Eastern Canada. *Engineering Geology*, *43*(1), 31–44. https://doi.org/10.1016/0013-7952(96)00031-2

Pollard, W. H. (1990). The nature and origin of ground ice in the Herschel Island area, Yukon Territory. In *Paper presented at 5th Canadian Permafrost Conference, Québec*.

Pufahl, D. E., & Morgenstern, N. R. (1979). Stabilization of planar landslides in permafrost. *Canadian Geotechnical Journal*, *16*(4), 734–747. https://doi.org/10.1139/t79-081

Rachold, V., Grigoriev, M. N., Are, F. E., Solomon, S., Reimnitz, E., Kassens, H., & Antonow, M. (2000). Coastal erosion vs riverine sediment discharge in the Arctic Shelf seas. *International Journal of Earth Sciences*, *89*(3), 450–460. https://doi.org/10.1007/s005310000113

Ramage, J. L., Fortier, D., Hugelius, G., Lantuit, H., & Morgenstern, A. (2019). Distribution of carbon and nitrogen along hillslopes in three valleys on Herschel Island, Yukon Territory, Canada. *Catena*, *178*, 132–140. https://doi.org/10.1016/j.catena.2019.02.029

Ramage, J. L., Irrgang, A. M., Herzschuh, U., Morgenstern, A., Couture, N., & Lantuit, H. (2017). Terrain controls on the occurrence of coastal retrogressive thaw slumps along the Yukon Coast, Canada. *Journal of Geophysical Research: Earth Surface*, *122*(9), 1619–1634. https://doi.org/10.1002/2017JF004231

Ramage, J. L., Irrgang, A. M., Morgenstern, A., & Lantuit, H. (2018). Increasing coastal slump activity impacts the release of sediment and organic carbon into the Arctic Ocean. *Biogeosciences*, *15*(5), 1483–1495. https://doi.org/10.5194/bg-15-1483-2018

Rampton, V. N. (1982). Quaternary geology of the Yukon coastal plain. *Geological Survey of Canada Bulletin*, *317*, 1–49.

Razumov, S. O., Spektor, V. B., & Grigoriev, M. N. (2014). Model of the post-Cenozoic evolution of the cryolithozone of the shelf of the western part of the Laptev Sea. *Oceanology*, *54*(5), 637–649. https://doi.org/10.1134/S0001437014040092

Rudy, A. C. A., Lamoureux, S. F., Kokelj, S. V., Smith, I. R., & England, J. H. (2017). Accelerating thermokarst transforms ice-cored terrain triggering a downstream cascade to the ocean. *Geophysical Research Letters*, *44*(21), 11080–11087. https://doi.org/10.1002/2017GL074912

Segal, R. A., Lantz, T. C., & Kokelj, S. V. (2016). Acceleration of thaw slump activity in glaciated landscapes of the Western Canadian Arctic. *Environmental Research Letters*, *11*(3), 034025. https://doi.org/10.1088/1748-9326/11/3/034025

Séjourné, A., Costard, F., Fedorov, A., Gargani, J., Skorve, J., Massé, M., & Mège, D. (2015). Evolution of the banks of thermokarst lakes in Central Yakutia (Central Siberia) due to retrogressive thaw slump activity controlled by insolation. *Geomorphology*, *241*, 31–40. https://doi.org/10.1016/j.geomorph.2015.03.033

Shepelev, A. G., Kizyakov, A., Wetterich, S., Cherepanova, A., Fedorov, A., Syromyatnikov, I., & Savvinov, G. (2020). Sub-surface carbon stocks in northern taiga landscapes exposed in the Batagay megaslump, Yana upland, Yakutia. *Land*, *9*(9), 305. https://doi.org/10.3390/land9090305

Smith, S., & Burgess, M. M. (2000). *Ground temperature database for northern Canada* (Vol. 3954, p. 57). Geological Survey of Canada Open File Report.

Stephani, E., Musial, M., & Anderson, S. (2015). Reclamation of material sites in continuous permafrost of Alaska; an example of groundwater flow between pits. In *Paper presented at 68th Canadian Geotechnical Conference and 7th Canadian Permafrost Conference; GEOQuébec 2015, Québec City, Québec, September 20–23 2015*.

Tanski, G., Lantuit, H., Ruttor, S., Knoblauch, C., Radosavljevic, B., Strauss, J., et al. (2017). Transformation of terrestrial organic matter along thermokarst-affected permafrost coasts in the Arctic. *Science of the Total Environment*, *581–582*, 434–447. https://doi.org/10.1016/j.scitotenv.2016.12.152

Telford, W. M., Geldart, L. P., & Sheriff, R. E. (1990). *Applied Geophysics* (p. 770). University Press.

Turetsky, M. R., Abbott, B. W., Jones, M. C., Anthony, K. W., Olefeldt, D., Schuur, E. A. G., et al. (2020). Carbon release through abrupt permafrost thaw. *Nature Geoscience*, *13*(2), 138–143. https://doi.org/10.1038/s41561-019-0526-0

Ward Jones, M. K., Pollard, W. H., & Jones, B. M. (2019). Rapid initialization of retrogressive thaw slumps in the Canadian high Arctic and their response to climate and terrain factors. *Environmental Research Letters*, *14*(5), 055006. https://doi.org/10.1088/1748-9326/ab12fd

Wetterich, S., Kizyakov, A. I., Opel, T., Grotheer, H., Mollenhauer, G., & Fritz, M. (2023). Ground-ice origin and age on Herschel Island (Qikiqtaruk), Yukon, Canada. *Quaternary Science Advances*, *10*, 100077. https://doi.org/10.1016/j.qsa.2023.100077

You, Y., Yu, Q., Pan, X., Wang, X., & Guo, L. (2017). Geophysical imaging of permafrost and talik configuration beneath a thermokarst lake. *Permafrost and Periglacial Processes*, *28*(2), 470–476. https://doi.org/10.1002/ppp.1938

Zwieback, S., Kokelj, S., Günther, F., Boike, J., Grosse, G., & Hajnsek, I. (2018). Sub-seasonal thaw slump mass wasting is not consistently energy limited at the landscape scale. *The Cryosphere*, *12*(2), 549–564. https://doi.org/10.5194/tc-12-549-2018